UNSTEADY AERODYNAMIC CALCULATIONS OF FLAPPING WING MOTION

A THESIS SUBMITTED TO
THE GRADUATE SCHOOL OF NATURAL AND APPLIED SCIENCES
OF
MIDDLE EAST TECHNICAL UNIVERSITY

BY

BUŞRA AKAY

IN PARTIAL FULFILLMENT OF THE REQUIREMENTS
FOR
THE DEGREE OF MASTER OF SCIENCE
IN
AEROSPACE ENGINEERING

SEPTEMBER 2007

Approval of the thesis:

UNSTEADY AERODYNAMIC CALCULATIONS OF FLAPPING WING MOTION

Submitted by BUŞRA AKAY in partial fulfillment of the requirements for the degree of **Master of Science in Aerospace Engineering Department, Middle East Technical University** by,

Prof. Dr. Canan Özgen _____
Dean, Graduate School of **Natural and Applied Sciences**

Prof. Dr. İsmail H. Tuncer _____
Head of Department, **Aerospace Engineering**

Prof. Dr. H. Nafiz Alemdaroğlu
Supervisor, **Aerospace Engineering Dept., METU** _____

Examining Committee Members:

Prof. Dr. Yusuf Özyörük _____
Aerospace Engineering Dept., METU

Prof. Dr. H. Nafiz Alemdaroğlu _____
Aerospace Engineering Dept., METU

Assoc. Prof. Dr. Serkan Özgen _____
Aerospace Engineering Dept., METU

Prof. Dr. Kahraman Albayrak _____
Mechanical Engineering Dept., METU

Assoc. Prof. Dr. Altan Kayran _____
Aerospace Engineering Dept., METU

Date: 06 / 09 / 2007

I hereby declare that all information in this document has been obtained and presented in accordance with academic rules and ethical conduct. I also declare that, as required by these rules and conduct, I have fully cited and referenced all material and results that are not original to this work.

Name, Last name: BUŞRA AKAY

Signature :

ABSTRACT

UNSTEADY AERODYNAMIC CALCULATIONS OF FLAPPING WING MOTION

AKAY, Buşra

M.Sc., Department of Aerospace Engineering

Supervisor: Prof. Dr. H. Nafiz Alemdaroğlu

September 2007, 89 pages

The present thesis aims at shedding some light for future applications of μAVs by investigating the hovering mode of flight by flapping motion. In this study, a detailed numerical investigation is performed to investigate the effect of some geometrical parameters, such as the airfoil profile shapes, thickness and camber distributions and as well as the flapping motion kinematics on the aerodynamic force coefficients and vortex formation mechanisms at low Reynolds number. The numerical analysis tool is a DNS code using the moving grid option. Laminar Navier-Stokes computations are done for flapping motion using the prescribed kinematics in the Reynolds number range of 10^1-10^3. The flow field for flapping hover flight is investigated for elliptic profiles having thicknesses of 12%, 9% and 1% of their chord lengths and compared with those of NACA 0009, NACA 0012 and SD 7003 airfoil profiles all having chord lengths of 0.01m for numerical computations. Computed aerodynamic force coefficients are compared for these profiles having different centers of rotation and angles of attack. NACA profiles have slightly higher lift coefficients than the ellipses of the same t/c ratio. And one of the most important conclusions is that the use of elliptic and NACA profiles with 9% and 12% thicknesses do not differ much as far as the aerodynamic force coefficients is concerned for this Re number regime. Also,

two different sinusoidal flapping motions are analyzed. Force coefficients and vorticity contours obtained from the experiments in the literature and present study are compared. The validation of the present computational results with the experimental results available in the literature encourages us to conclude that present numerical method can be a reliable alternative to experimental techniques.

Keywords: Flapping Motion, Unsteady Aerodynamics, CFD

ÖZ

ÇIRPAN KANAT HAREKETİNİN ZAMANA BAĞLI AERODİNAMİK HESAPLAMALARI

Akay, Buşra

Yüksek Lisans, Havacılık ve Uzay Mühendisliği Bölümü

Tez Yöneticisi: Prof. Dr. H. Nafiz Alemdaroğlu

Eylül 2007, 89 sayfa

Bu tez çırpan kanat hareketinin havada asılı kalma modunu inceleyerek gelecekteki mikro hava araçları uygulamalarına ışık olmayı amaçlamıştır. Bu çalışmada, düşük Reynolds sayısında kanat kesitinin şekli, kalınlığı, kambur dağılımı gibi geometric parametrelerin ve bunların yanında çırpan kanat hareketinin aerodinamik kuvvet katsayılarının ve girdap oluşum mekanizmasının üzerindeki etkilerini araştırmak için detaylı bir sayısal inceleme gerçekleştirilmiştir. Sayısal analiz aracı hareket eden ağ yapısı opsiyonunu kullanabilen bir DNS koddur. Laminar, Navier-Stokes hesaplamaları belirlenen kinematikler kullanılarak çırpan kanat hareketleri için 10^1-10^3 Reynolds sayısı rejimi içinde gerçekleştirilmiştir. Çırpan kanat hareketinin havada asılı kalma modunda akış alanı kalınlıları vetere uzunluklarının (c=0.01m) %12, %9 and %1 olan eliptik profiler için araştırılmıştır ve vetere uzunlukları 0.01m olan NACA 0009, NACA 0012 and SD 7003 kanat kesitleri ile karşılaştırılmıştır. Hesaplanan aerodinamik kuvvet katsayıları bu profillerin farklı dönme noktaları ve hücum açıları için karşılaştırılmıştır. Aynı t/c oranı için NACA profilleri elipslerden biraz daha fazla kaldırma kuvveti katsayısına sahip olmuşlardır. En öenmli sonuçlardan biri de bu Reynolds sayısı rejimi için aerodinamik kuvvet katsayıları düşünüldüğünde %9 ve %12 kalınlıktaki NACA ve eliptik profil kullanmanın fazla

bir farkı olmadığıdır. Aynı zamanda iki farklı sinusoidal çırpan kanat hareketi incelenmiştir. Literatürdeki deney sonuçlarından sağlanan kuvvet katsayıları ve girdap konturları ile bu çalışmadan elde edilen sonuçlar karşılaştırılmıştır. Bu çalışmadan elde edilen sayısal sonuçların literaturdeki deneysel sonuçlar ile sağlanmış olması bizi ‘bu çalışmadaki sayısal metod deneysel tekniklere güvenilir bir alternatif olabilir’ sonucuna götürmüştür.

Anahtar Kelimeler: Çırpan Kanat Hareketi, Zamana Bağlı Aerodinamik, CFD

to the proprietor of everything...

ACKNOWLEDGEMENTS

I wish to state my thanks to my supervisor Prof. Dr. H. Nafiz Alemdaroğlu for his support, advice, guidance and criticism during this thesis.

I also wish to state my sincere thanks to Dr. D. Funda Kurtuluş to act as a co-supervisor. She assists me during all stages of this study. She always encourages me to work hard and to put a good performance throughout this study. I am beholden her for every step of my thesis study.

I also thank to jury members Assoc. Prof. Dr. Serkan Özgen and Assoc. Prof. Dr. Altan Kayran to review my thesis.

I also thank to my mother for her advice, guidance and endless support. If she did not support me in all stages of my life, I would not be here. Thank God that I have Necla. I also thank to my father, my sisters and my brother.

I also thank to my friends Serpil, Samih, Özgür, Deniz, Özlem, Tahir, Evrim, Monier, and Serhan for their endless support.

I also thank to Ms. Figen, Ms. Derya and Mrs. Nilgun for their support during this thesis.

This study was supported by 104M417 TUBITAK project.

TABLE OF CONTENTS

LIST OF TABLES

LIST OF FIGURES

CHAPTER I

INTRODUCTION

This thesis is about numerical analysis of two dimensional flapping motion in hovering mode. Direct Numerical Simulation is used to solve the flow field around the two dimensional wing during the flapping motion. Unsteady, laminar, incompressible two dimensional Navier-Stokes Equations are solved by using moving grid technique. After grid refinement studies, O type grids are generated around the profiles with grid outer boundaries chosen to be at 20 chord lengths.

The flapping motion is assumed to consist of a downstroke, rotation and an upstroke. The length of each stroke depends on the kinematics of the defined flapping motion. Detailed information about flapping kinematics is given in the following chapters. Three types of flapping motion kinematics are analyzed during this thesis study and their descriptions are given in Chapter III.

The first motion type is prescribed by Kurtulus et al. [1]. A parametric study is performed on the unsteady aerodynamics of different wing profiles at low Reynolds number (Re=1000) with this flapping motion kinematics [1]. An investigation is done to assess the importance of the shape and thickness of the 2D wing profile on the aerodynamic force coefficients and the vortex formation mechanisms by using the Direct Numerical Simulation technique. The profiles investigated are elliptic profiles with 12%, 9% and 1% thicknesses and NACA 0009, NACA 0012 and SD 7003 airfoil profiles all having 0.01m chord lengths. The computed aerodynamic force coefficients are then compared for these profiles for different center of rotations and angles of attack [2].

The second and third flapping motion kinematics are prescribed by Wang et al. [3] and Freymuth [4]. A study is performed to check the computational performance of the present numerical method and to analyze the sinusoidal flapping motion aerodynamics for different Reynolds numbers in the range 10^1-10^3 by using this kinematics. Two different sinusoidal motions are simulated by implementing the sinusoidal translational and angular motions using the same numerical solver.

The present thesis is composed of 5 Chapters. The theoretical background of the present study and a review of the literature about flapping motion are given in Chapter 2. In Chapter 3, the numerical method is explained by giving the computational details and by describing the wing models and the kinematics used. The computational results obtained by using the DNS code are given in Chapter 4. Finally, the conclusions obtained from the present investigations are given in Chapter 5.

CHAPTER II

BACKGROUND OF THE STUDY

Interest in the aerodynamics of insect flights has increased in conjunction with the concept of Micro Air Vehicles (μAVs). Based on their size, flying insects operate in a wide range of Reynolds numbers; from approximately 10^1 to 10^5 [5]. Operating Reynolds number ranges of μAVs are similar with those of birds or insects. Thus, this similarity led most of the researchers to understand the aerodynamic basis for the flight of birds and insects.

The present study aims at shedding some light for future applications of μAVs by investigating the hovering mode of flight by flapping motion.

2.1 Basic Aerodynamics of Insect Flight

Four degrees of freedom in each wing are used to achieve flight in nature: flapping, lagging, feathering and spanning. Flapping is an angular movement about an axis in the direction of flight. Lagging is an angular movement about a vertical axis which effectively moves the wing forward and backward parallel to the vehicle body. Feathering is an angular movement about an axis around the center of the wing which tilts the wing to change its angle of attack. Spanning is an expanding and contracting of the wing span. However not all flying animals can implement all of these motions. Unlike birds, most insects do not use the spanning. They have very restricted lagging capabilities. Thus, flapping flight is possible with only two degrees of freedom: flapping and feathering [6].

The critical characteristic in insect flight which distinguishes it from other flying creatures or machines is the kinematics of wing motion (except for hummingbirds).

Due to their smaller scale, insects differ fundamentally from birds. Insects carry out all of the operations at their wing roots. As a result of this kinematics, the aerodynamics associated with insect flight is also very different from those encountered in conventional fixed- and rotary-wing or even bird flight [7].

Figure 2.1 Hummingbird [8].

Identification of major forces is critical to understand insect flight. Conventional aerodynamic theory is based on rigid wings moving at constant velocity. However, it is observed that when insect wings are placed in a wind tunnel and tested over a range of air velocities, the measured forces generated by flapping their wings are substantially smaller than those required for active flight [9]. Thus, there is something more complex with the flapping motion which increases the lift produced by a wing. The failure of conventional steady-state theory has prompted the search for unsteady mechanisms that might explain the origin of these high forces produced during flapping motion [10].

2.1.1 Hovering Flight

"Hovering is an extreme mode of flight where the forward velocity is zero. To do this, insects must draw clean air from the ambient flow and get rid of the `messy vortices' they have created to obtain a large periodic lift" [11].

The wingstroke of an insect is divided into four stages: while the wings sweep through the air with a high angle of attack, two translational phases (upstroke and downstroke) occur; and while the wings rapidly rotate and reverse direction, two rotational phases (pronation and supination) occur [12]. The wing path is shown with a blue dotted line. Blue arrows indicate the direction of the wing motion. Lift (dark blue) and drag (green) aerodynamic forces are components of the total aerodynamic force (red).

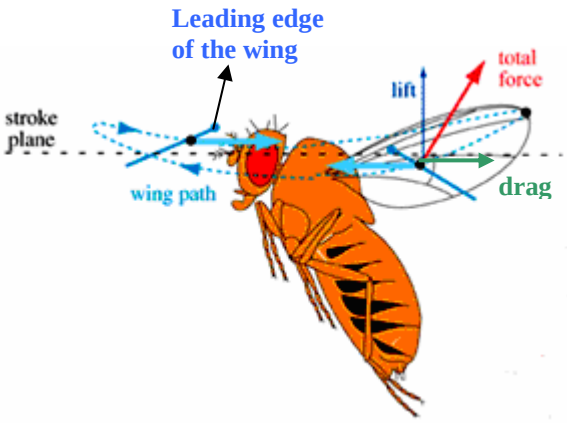

Figure 2.2 Hovering flight posture [12].

A hovering hummer keeps its body at about a 45^{o} angle to the ground and moves its wings in a more or less a "figure eight" pattern. Hummers have an extremely mobile shoulder joint to generate lift on both up-downstrokes. The direction of thrust changes between the up-downstrokes, so that they cancel each other out. Since the wings beat more than 20 times per second (sometimes as rapidly as 80 beats per second), inertia holds the bird's body essentially stationary [13].

However, the hovering flight is quite expensive. While weak fliers and strong flying birds invest about 15 and 20 percent (respectively) of the total body weight in the breast muscles, hummingbirds invest about 30 percent of the total body weight in the breast muscles [13].

The flow associated with insect flapping flight is incompressible, laminar and unsteady, and occurs at low Reynolds numbers (10^1 – 10^5). The enhanced aerodynamic performance of insects result from an interaction of some mechanisms: Wagner effect, delayed stall and the formation of leading edge vortex, Kramer effect, wake capture, and clap and fling mechanism.

2.1.2 Wagner Effect

There are three main features in insect's flapping cycle. These are the wing's repeated acceleration (starting), deceleration (stopping) and reversal. "This 'start–stop–reversal' behavior is fundamental to the aerodynamics that makes this flight possible [7]." During this process, vorticity is generated and shed at the trailing edge, and the shed vorticity eventually rolls up in the form of a starting vortex. The vorticity shed at the trailing edge induces a velocity field in the vicinity of the wing. This velocity field counteracts the growth of circulation bound to the wing and therefore, has an inhibitory effect on lift-the so-called Wagner effect. Until the starting vortex has moved sufficiently far from the trailing edge, this effect proceeds. Then the wing attains its maximum steady circulation (see Figure 2.3). As it is seen in Figure 2.3, the ratio of instantaneous to steady circulation grows as the trailing edge vortex moves away from the airfoil, and its influence on the circulation around the airfoil diminishes with distance [5].

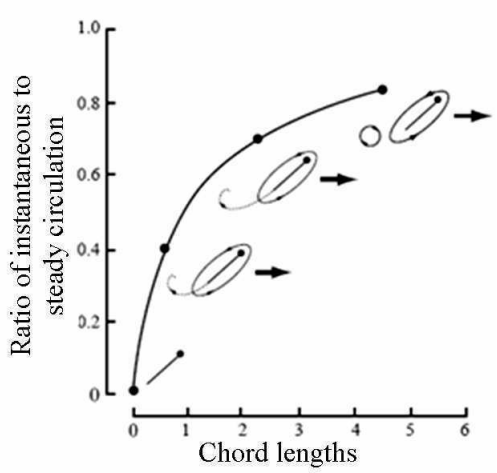

Figure 2.3 Schematic diagram of Wagner effect. Distance is non-dimensionalized with respect to chord lengths traveled [5].

2.1.3 Delayed Stall and Leading Edge Vortex

Delayed stall occurs during the translational phase of the stroke. As the wing increases its angle of attack, the fluid stream going over the wing separates as it crosses the leading edge but reattaches before it reaches the trailing edge. In such cases, a leading edge vortex occupies the separation zone above the wing. Because the flow reattaches, the fluid continues to flow smoothly from the trailing edge and the Kutta condition is maintained. In this case, because the wing translates at a high angle of attack, a greater downward momentum is imparted to the fluid, resulting in substantial enhancement of lift [5].

Although many mechanisms are identified to explain the insect flight, the main source of the extra lift was unknown until Ellington et al. [14] discovered the leading edge vortex. They have visualized the airflow around the wings of the Hawkmoth Manduca sexta and a hovering large mechanical model –the flapper. An intense leading edge vortex having sufficient strength to explain the high lift forces was found on the downstroke. The vortex is created by dynamic stall, and not by the rotational lift mechanisms that have been postulated for insect flight. The schematic representation of delayed stall is given in Figure 2.4-(1).

2.1.4 Kramer Effect (Rotational Circulation)

Insect wings generate lift during both up and down strokes by always having positive angle of attack. This is achieved by undergoing substantial two rotational phases (pronation and supination) about a spanwise axis near the end of every stroke [5]. The orientation of the resulting force should also depend critically on the direction of wing rotation. If the wing flips early, before reversing direction, then the leading edge rotates backward relative to translation set of simplified wing kinematics. An advance in rotation relative to translation results in a positive lift peak at the end of each half stroke, whereas a delay in rotation results in negative lift at the beginning of each half stroke. Thus, by properly adjusting the timing of wing rotation, an insect can generate lift via a rotational mechanism in excess of that produced by delayed stall [5].

According to Dickinson et al. [10], the physics of rotating wings have two important consequences for the forces generated by rotational circulation due to flat insect wings. First, the rotational force on a wing acts normal to its chord, not perpendicular to the direction of motion. Second, viscous forces within the air will make the flow smoothly at the sharp trailing edge. This constraint, termed the Kutta condition, fixes a fluid stagnation point at the trailing edge of the wing. The functional consequence of the Kutta condition is that the amount of circulation and thus force produced by a rotating wing will depend critically upon the position of the rotational axis [10]. The schematic representation of rotational lift is given in Figure 2.4-(2). At its completion (see Figure 2.4-(3)), the maneuver also results in a powerful force propelling the insect forward.

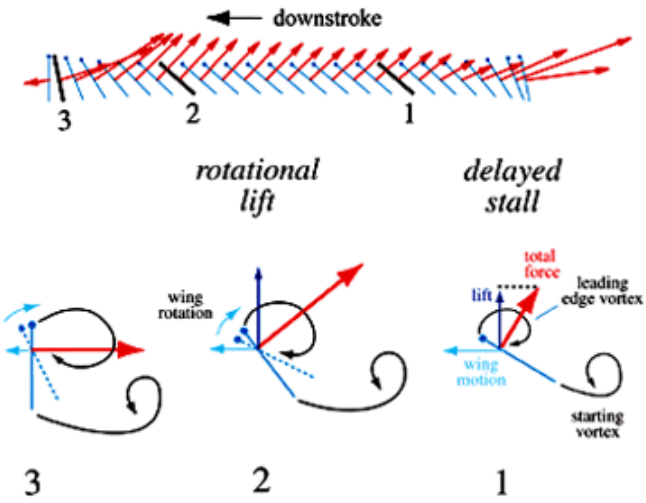

Figure 2.4 Schematic representation of delayed stall and rotational lift. A fly moves from right to left during a downstroke of its wings *(top)*, blue arrows indicate the direction of wing movement and red arrows the direction and magnitude of the forces generated in the stroke plane [12].

2.1.5 Wake Capture

The wake behind a flying object contains energy imparted to the surrounding fluid in the form of momentum and heat. Wing passage through the wake could, therefore, be a method to recover some of this lost energy (wake from previous stroke) and utilize it usefully for flight [6]. The schematic representation of wake capture is given in Figure 2.5 (1, 2).

According to Dickinson et al. [10], although rotational circulation can explain one of the stroke reversal forces, it can not explain the large positive transient that develops immediately after the wing changes direction at the start of each half stroke. These force peaks are distinct from the rotational circulation peaks, because their timing is independent of the phase of wing rotation. One possible explanation for these forces is the mechanism of wake capture, in which the wing benefits from the shed vorticity of the wing at an angle that produces negative lift.

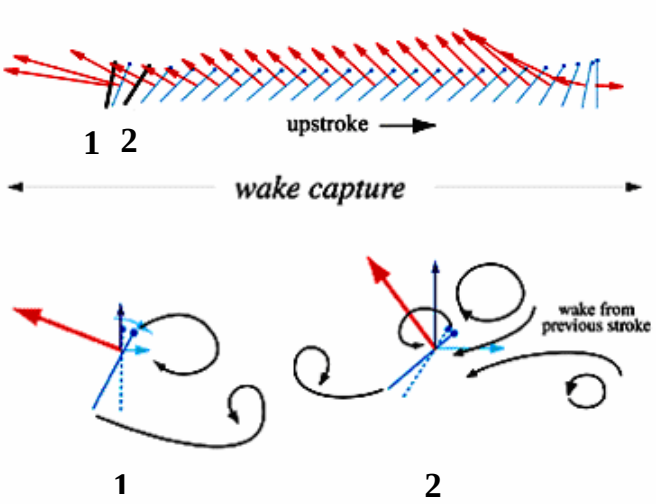

Figure 2.5 Schematic representation of wake capture. A fly moves from left to right during a upstroke *(top)*, blue arrows indicate the direction of wing movement and red arrows the direction and magnitude of the forces generated in the stroke plane [12].

2.1.6 Clap and Fling Mechanism

The clap-and-fling mechanism was first proposed by Weis-Fogh [15] to explain the high lift generation in the chaliced wasp *Encarsia formosa* and is sometimes also referred to as the Weis-Fogh mechanism [5].

In this process, the wings clap together above the insect's body and then fling apart. As they fling open, the air gets sucked in and creates a vortex over each wing. This bound vortex then moves across the wing and, in the clap, acts as the starting vortex for the other wing. By this method, circulation and thus lift are increased to the extent of being higher, in most cases, than the typical leading edge vortex mechanism [16]. "Although the clap and fling may be important, especially in small species, it is not used by all insects and thus can not represent a general solution to the enigma of force production [10]." In Figure 2.6 schematic representation of clap and fling mechanism is presented. Black lines show flow lines, and dark blue arrows show induced velocity. Light blue arrows show net forces acting on the airfoil.

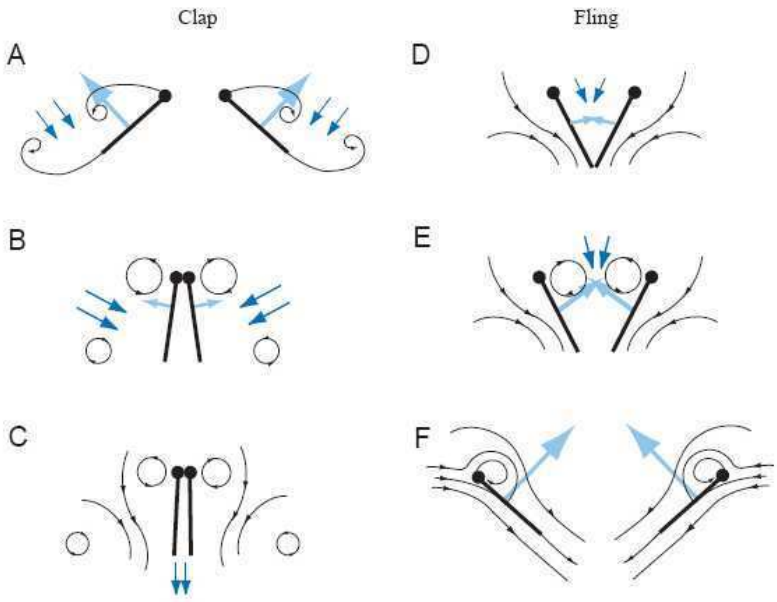

Figure 2.6 A-C represent wing approaching each other to clap and D-F represent flinging apart [5].

2.2 Advantages of Flapping Flight in MAV

Insect-like flapping wing Micro Air Vehicles (μAVs) are small hand-held flying vehicles that are developed for the purpose of reconnaisance in confined spaces, for example, inside buildings, tunnels and shafts. To perform these applications, the vehicles have a stable hover and a highly maneuverable power efficient platform. Flying insects have this kind of performance, and hence, insect-like flapping is focused on by engineering means [17].

“The flapping motion of insect wings is qualitatively different from fixed airplane wings or even the rotation of helicopter blades.” It's perhaps not surprising, that the quasi-steady-state analysis that works so well for aircraft but it does not work when insects’ flight is considered [18]. Although flapping wing design is more complex than a fixed wing design, there are many reasons to explore the possibilities of flapping wing flight.

- The size constraints:

While the vehicle becomes smaller, the fixed wing application becomes less reasonable. The lift which a fixed wing generates to support the weight of the vehicle is directly proportional to wing area and velocity of air flow over the wing. Thus, the smaller the vehicle, the less lift it can supply.

- To increase lift -to support the weight of the vehicle- most designs increase the velocity of the vehicle. Increasing velocity is unacceptable in situations such as indoor missions where a μAV makes the most sense.

- A flapping wing design can rely on lift generated by airflow created by both vehicle speed and wing flapping to support the weight of the vehicle. Therefore, if the scale is reduced, the frequency of the beating can be increased without affecting the minimum velocity of the vehicle [6]. The main consequence for insect flight is generation of high lift at low speeds thus enabling slow, but highly maneuverable and power efficient flight [19].

- Ability to perform short takeoffs and landings:

Provided with enough power, a vehicle with flapping wings could actually takeoff and land vertically [6].

Figure 2.7 Sympetrum flaveolum-side (aka) [16].

2.3 Literature Survey

The aim of the present section is to combine the studies performed about the flapping motion in recent years. This literature survey will help to understand the fundamentals of the flapping flight. While surveying the literature, the studies are divided into three subgroups; experimental studies, numerical studies, and comparative studies.

2.3.1. Numerical Studies

The defining property of airfoil aerodynamics at low Reynolds number is laminar flow separation. Many applications have been performed by using Navier-Stokes solvers in the field of flapping motion. NACA 0012 airfoil profile has been used as wing section in many applications ([20]-[23]) with pure pitching and combined pitch-plunge oscillations. Tuncer and Kaya [20] have investigated sinusoidal plunge and pitching motion by using unsteady laminar and turbulent flow in a wide range of Re number; $10^4<Re<10^6$. Young and Lai [21] have analyzed sinusoidally oscillating NACA 0012 airfoil in plunge motion at $Re=2x10^4$. They have also used unsteady panel method (UPM) with numerical visualization using the partical tracing method. Later, Young [22] have used unsteady panel method and Navier-Stokes solver codes to analyze plunging and pitching airfoil at Re=12000. 2D airflow of a stationary/flapping airfoil combination in tandem has been investigated by using Navier-Stokes solver with Baldwin-Lomax and Baldwin-Barth turbulence models [23]. To provide more insight into the bioaerodynamics of insect flight for the design of flapping wing MAVs, Szmelter and Zbikowski [19] have analyzed 3D bibio fly wing at Re number higher than $9x10^3$ by using NACA 0012 profile. The kinematic data used in this study was provided by Willmott and Ellington ([24]-[26]). A detailed analysis of free flight in the hawkmoth *Manduca sexta* has revealed the kinematic changes as the speed increases from hovering to fast forward flight. It was observed that significant changes occurred in the aerodynamics of the observed kinematic variation, the power requirements for flight at different speeds and the

nature of the constraints on maximum flight speed ([24], [25]). According to Willmott and Ellington, a robust technique for determining the angle of attack of insect wings is to use a fast camera to film the free flight. To date this method has proved to be elusive. They reported a study describing the development of two new methods – the Strips and Planes techniques – which were designed to overcome some of the limitations experienced in previous studies ([26]).

Three dimensional hovering flight of the dragonfly in tandem configuration at Reynolds number of the order of 10^3 have been analyzed by Isogai et al. [27]. They used a Navier-Stokes code and validated their results by comparing their simulations with the experimental values of total lift and stroke plane angle obtained using a flying robot.

Wu and Sun [28] have analyzed flapping motion of the fruit fly wing with flat plate wing section in the range of $20<Re<1800$. They analyzed the effects of varying five non-dimensional parameters (i.e. Reynolds number, stroke amplitude, mid-stroke angle of attack, non-dimensional duration of wing rotation, rotation timing) on the force coefficients were analyzed.

Miller and Peskin [29] used immersed boundary method to solve the two-dimensional Navier–Stokes equations for two immersed wings performing an idealized clap and fling stroke and a fling half-stroke in the range of $8<Re<128$. They found that flow around the wing branches into two distinct patterns. For $Re>64$, leading and trailing edge vortices are alternately shed behind the wing forming the Karman vortex street. For $Re<32$, the leading and trailing edge vortices remain attached to the wing during each half stroke.

Ramamurti and Sandberg [30] have used finite element flow solver to analyze 3D drosophila wing in flapping motion at Re=136. The effect of phasing between the translational and rotational motions was studied by varying the rotational motion prior to the stroke reversal.

Elliptic profiles have also been used to investigate the flapping motion characteristics ([31]-[34]). Lan and Sun [31] explored the flapping motion at Re=1000 by using a Navier-Stokes solver for incompressible flow implementing moving overset grid. The results show that, if the insect employs a larger angle of attack or changes the timing of wing rotation, much greater lift can be produced for maneuvering and for other purposes. 3D flapping motion of the model fruit fly wing at Re=136 has been investigated by Sun and Tang [32] with some insights into the unsteady aerodynamic force generation process from the force and flow-structure information. They compared their results with the model wing experimental results and fruit-fly data provided by Dickinson et al. [10] and Weis-Fogh [15]. Weis-Fogh [15] aimed to provide new material and novel solutions to make use of the large number of observations on freely flying animals. His major conclusion is that most insects perform normal hovering on the basis of the well-established principles of steady-state flow. However, one must also realize that any type of flapping flight involves also non-steady periods, particularly at the reversal points where active pronation and supination occur. Wang ([11], [33]) has analyzed 2D hovering and flapping flight on elliptic wing section to identify the vortex shedding and their frequencies in the Re number range of $10^2<Re<10^4$. Eldredge [34] has performed DNS solutions with viscous vortex particle method to investigate the pitching and plunging motion at Re=550.

2.3.2. Experimental Studies

The understanding the physics of flapping flight has long been limited due to the obvious experimental difficulties in studying the flow field around real insects. Recently, PIV and DPIV techniques have been used as novel experimental tools to analyze the flapping motion [35] - [37].

Poelma et al. [35] have performed a 3D Steoreoscopic PIV experiment in a mineral oil tank to measure the time dependent three-dimensional velocity field quantitatively, around a dynamically scaled robotic flapping wing at Re=256.

For the first time it was shown that data can also be obtained for quantitative studies, such as lift and the drag. Tian et al. [36] have implemented the PIV technique by using a fog generator in a flight cage to understand the 3D high speed stereo images to analyze the kinematic motion during straight and turning flights of a bat in the Re number range of 10^4<Re<10^5. The kinematic data revealed that, at relatively slow flight speeds the wing motion is quite complex, including a sharp retraction of the wing during the upstroke and a broad sweep of the fully extended wing during the downstroke. Clap and fling movement have been analyzed using dynamically scaled mechanical model of the small fruit fly Drosophila melanogaster (see Figure 2.8) by Lehmann et al. [37]. They performed 3D DPIV experiments and used force transducers to investigate force enhancement due to contra lateral wing interactions during stroke reversals (‘the clap-and-fling’) in the Reynolds number range of 100<Re<200.

Figure 2.8 Drosophila_melanogaster-side [16].

Figure 2.9 A, B shows time sequences of one wing stroke cycle with superimposed instantaneous force vectors produced by an isolated single wing. In this case, the mean flight force normal to the wing surface and averaged throughout the entire stroke cycle is approximately 0.453 N, with a peak at the beginning of the down stroke of 1.34 N. In comparison, a wing undergoing the same kinematic pattern along with a second, mirror-image symmetric wing produces a mean force of approximately 0.476 N, with a peak of 1.82 N (Figure 2.9 C, D). The results of this study on the dorsal clap-and-fling mechanism in flapping wing motion of ‘hovering’

robotic fruit fly wing has revealed an unknown complexity of flight force modifications throughout the entire stroke [37].

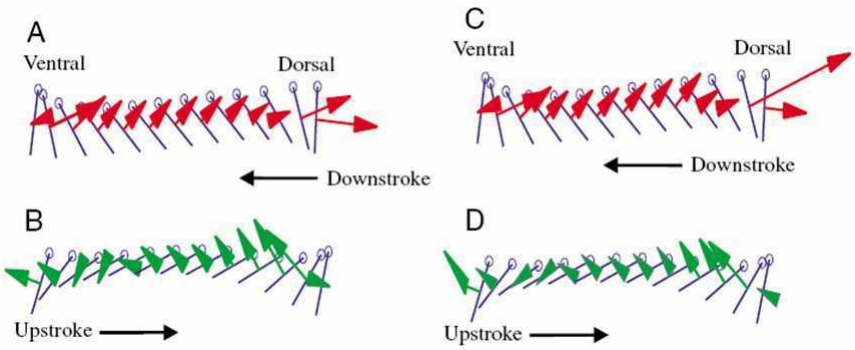

Figure 2.9 Wing motion of a robotic wing performing a clap-and fling kinematic maneuver [37].

Galvao et al. [38] have explored 3D mammalian flight with compliant membrane wing models in the range of 70000<Re<200000. They have used a low-speed, low turbulence wind tunnel equipped with a stereo photogrammetric system.

2D biomimetic flapping-pitching wing is analyzed by Singh et al. [39] using laser sheet visualization method at Re=15000. Images were captured by a CCD camera, and the seeding was produced by vaporizing a mineral oil into a dense fog.

Usherwood et al. [40] have investigated the flight of Pigeons in slow, flapping flight to obtain the dynamic pressure maps of their wings and tails by using accelerometers and differential pressure sensors.

Dickinson et al. [10] have performed an experiment in a mineral oil tank with a 3D dynamically scaled model of the fruit fly to investigate the interaction of three distinct interactive mechanisms namely delayed stall, rotational circulation, and wake capture on the enhancement of the aerodynamic performance of insect flights. Experiments have been performed at Re=136. The wing was equipped with a 2D force transducer. Before this study, Dickinson and Götz [41] have performed similar

experiments in an aquarium by using a 2D impulsively moved model wing in the range of 10<Re<1000. The purpose of Dickinson and Götz's [41] analysis is not to drive yet another nail into the quasi-steady state coffin, but rather to characterize the time-dependency of forces produced by impulsively moved wings and thereby expand the knowledge of unsteady mechanisms that might be employed by insects during flight. In particular, they were concerned with the time history of two processes: the generation of lift and the onset of stall. Time dependence of force production, the effect of Reynolds number on unsteady forces, effects of surface roughness and camber on force coefficients were analyzed. They concluded that the unsteady process of vortex generation at large angles of attack might contribute to the production of aerodynamic forces in insect flight.

Spedding et al. [42] performed a study reporting on the results of an extensive series of experiments in measuring bird wakes over a continuous range of flight speeds in a closed-loop, low-turbulence wind tunnel. The measurement technique has been customized extensively for this particular application. A correct reconstruction of the most likely three-dimensional wake structure is focused on.

Recent experimental and numerical unsteady aerodynamic research in the domain of flapping flight with applications to Micro Air Vehicles are also presented by Platzer and Jones [43] and the analytical models developed for insect-like flapping are summarized by Ansari et al. [7] with the basic aim of applying them to flight dynamic problems of Micro Air Vehicles.

2.3.3. Comparative Studies: Experimental vs. Numerical Approaches

There are many comparative studies available in the literature used mainly to validate the numerical studies in the field of flapping motion to understand the fundamentals of the aerodynamics of the flapping motion. Some of them is analyzed and presented below.

Kurtulus et al. [1] has performed a study to understand the aerodynamic mechanisms and vortex shedding dynamics of flapping motion by using numerical methods, analytical models and experimental techniques. The numerical study was investigated in three sub-section namely, numerical visualization, vortex identification via different methods and calculation of the instantaneous aerodynamic forces and average lift and drag coefficient values. In the experimental part of the study, the dimensional analysis for the air-water comparison, description of the displacement system, laser plane visualization and PIV measurement procedure were performed. The numerical and experimental visualizations are compared in order to understand the vortex generation mechanism during the motion in consideration and to reason the unsteady effects generated by these vortices on the airfoil in terms of the aerodynamic force coefficients and pressure distribution. The experimental results are done as a part for the validation of numerical simulations. The visualizations and Q contours are the indirect validation of the aerodynamic force calculations of these numerical solutions.

Pivkin et al. [44] have utilized arbitrary Lagrangian-Eulerian formulation of the incompressible Navier-Stokes equation to investigate the 3D airflow around the bat wings during flight at Re=100. They have also implemented an experiment by using two high speed cameras to track the infrared markers attached to the bat wings.

Another comparative study was performed by Wang et al. [3]. In this study, the computational, experimental and quasi-steady forces in a generic hovering wing undergoing sinusoidal motion along a horizontal stroke plane were compared. By using a dynamically scaled robotic fly, both force and flow data were obtained. At the base of one arm was attached a 2D force sensor that measured forces parallel and perpendicular to the wing surface. Lift and drag forces were then calculated from the perpendicular shear forces measured by the sensor. Digital Particle Image Velocimetry (DPIV) was used to measure the flow structure in a 841 cm^2 area centered on the wing. The oil was seeded with air forced through a ceramic water filter stone, creating a dense bubble field. The computational model used is a thin wing element of elliptic cross section undergoing the same kinematics as performed

in the experiments. The computation of flow around this hovering wing employs a fourth-order finite difference scheme of Navier–Stokes equation in vorticity-stream function formulation. Here it is seen that the success and failure of a 2D model in capturing the forces in 3D experiments can provide important insights. In both the advanced and symmetrical rotation cases, the 2D forces are very similar to the 3D forces. A notable difference between the experimental and computational forces is seen in the delayed rotation, where there is a clear phase shift between the computed and measured lift.

CHAPTER III

NUMERICAL METHODS

Any CFD, CAD or CAE system should be treated as a *tool* to assist the engineer in understanding physical phenomena. The success or failure of a fluid simulation depends not only on the code capabilities, but also upon the input data, such as:

- Geometry of the flow domain
- Fluid properties
- Boundary conditions
- Solution control parameters

For a simulation to have any chance of success, such information should be physically realistic and correctly presented to the analysis code.

By being aware of and completing these tasks, STAR-CD is chosen as a CFD tool and used in the numerical analysis part of this study. Direct Numerical Simulation (DNS) technique is used to solve the present flapping motion problems. The code has the capability to solve transient flow problems, use moving mesh with arbitrary motions, handle user defined properties and conditions by the use of user-defined subroutines, and it also has the capability of handling a large variety of boundary conditions, and offers a range of moving mesh features.

3.1 Flow Field Description

Transient time domain is applied to the problem, due to nature of the simulation. The transient calculation starts from well defined initial and boundary conditions and proceeds to a new state in a series of discrete time steps.

Direct Numerical Simulation is used to simulate the flow field. Because the Reynolds number is low, there is no need to apply a turbulence model. Simulation is performed for laminar, incompressible flow condition. The thermo-physical properties of the fluid (air) are specified as follows (see Table 3.1):

Table 3.1 Thermo-physical properties of the fluid

Density	Constant	1.225 kg/m3
Viscosity	Constant	1.781×10^{-5} kg/ms
Specific Heat	Constant	1006 J/kgK

The acronym PISO stands for ‘Pressure Implicit Splitting of Operators’ used for time dependent flows. PISO is mandatory for unsteady calculations where at each iteration (or time step) a predictor step is performed, followed by a number of corrector steps, during which linear equation sets are solved iteratively for each main dependent variable. Therefore, in this study Transient PISO solution procedure is used during the calculations. Scalar solver type and implicit temporal discretization is used by STAR-CD during these calculations with an Upward Differencing (UD) scheme [45].

The mass and momentum conservation equations are solved by STAR-CD for general incompressible and compressible fluid flows using a moving coordinate frame. The ‘Navier Stokes’ equations in Cartesian tensor notation [45] are:

$$\frac{1}{\sqrt{g}}\frac{\partial}{\partial t}(\sqrt{g}\rho)+\frac{\partial}{\partial x_j}(\rho\tilde{u}_j)=s_m \tag{3.1}$$

$$\frac{1}{\sqrt{g}}\frac{\partial}{\partial t}(\sqrt{g}\rho u_i)+\frac{\partial}{\partial x_j}(\rho\tilde{u}_j u_i-\tau_{ij})=-\frac{\partial p}{\partial x_i}+s_i \tag{3.2}$$

where t : time

x_i : cartesian coordinate (i=1,2,3)

u_i : absolute fluid velocity component in direction x_i

$\tilde{u}_j$: u_j-u_{cj}, relative velocity between fluid and local (moving) coordinate frame that moves with velocity u_{cj}

p : piezometric pressure = p_s- ρ_0 g_m x_m where p_s is static pressure, ρ_0 is reference density, the g_m are gravitational field components and the x_m are coordinates from a datum where ρ_0 is defined

ρ : density

τ_{ij} : stress tensor components

S_m : mass source

S_i : momentum source components

$\sqrt{g}$: determinant of metric tensor

In the case of laminar flows, STAR-CD caters for Newtonian fluid that obeys the following constitutive relation [45]:

$$\tau_{ij}=2\mu s_{ij}-\frac{2}{3}\mu\frac{\partial u_k}{\partial x_k}\delta_{ij} \tag{3.3}$$

where μ is the molecular dynamic fluid viscosity and , δ_{ij}, the ‘Kronecker delta’. It is unity when *i* = *j* and zero otherwise.

The rate of strain tensor is represented by S_{ij}, and is given by:

$$s_{ij} = \frac{1}{2}\left(\frac{\partial u_i}{\partial x_j} + \frac{\partial u_j}{\partial x_i} \right) \tag{3.4}$$

3.2 Definition of Boundaries

For unsteady flow simulation problems, specifying the location and definition of boundaries, transient boundary conditions and time steps are critically important. The boundary conditions and locations are determined as follows:

- **Pressure Boundaries**: In the case of pressure boundaries, the mass flow rates are unknown a priori and are determined as part of the solution. Pressure boundaries should be applied either in regions where the pressure is expected to be uniform (or nearly so) or where the variation is known. The farfield boundary is determined by pressure boundary condition. The pressures at the boundary cell faces are assumed known and taken to be the standard air pressure. To obtain the velocities at these faces, the velocities at these cell faces are linked to the local pressure gradients by momentum equations, whose coefficients are equated to those at the cell centre. These equations, together with the continuity constraint, effectively allow the magnitude and direction of the local flow (which may be inwards or outwards) to be calculated. The Pressure boundary location is shown in Figure 3.1.

- **Symmetry Plane Boundaries**: In STAR-CD, symmetry boundaries are used at two sides of the domain to get two dimensional solution (see Figure 3.1). No user input is required beyond definition of the boundary location. The normal component of velocity and the normal gradient of all other variables are set to zero at the boundary.

- **Wall Boundaries**: The Wall boundary condition is defined as no-slip, moving mesh type which is controlled by a user defined subroutine (see Figure 3.1).

The flapping motion kinematics is implemented on this wall boundary condition by using user defined subroutines. Three user defined subroutines are implemented into STAR-CD namely BCDEFW, UPARM, POSDAT.

BCDEFW.f: This subroutine enables the user to define boundary conditions at the wall for U, V, W, etc.

UPARM.f: Generates parameters required for moving meshes. This subroutine enables the user to generate parameters to be used by “prostar” when it is called during the execution of “egrid” in a moving mesh transient solution. Position of the model is determined in this subroutine.

POSDAT.f: Performs special post-processing operations. This subroutine enables the user record data and is called at the end of each iteration/time step. Aerodynamic forces and the other parameters like iteration number, time, and position of the model, velocity and angle of attack are written in this subroutine.

3.3 Wing Models Considered and Their Kinematics

Three types of flapping motion are analyzed during this thesis study. In the present study, the flapping motion prescribed by Kurtuluş et al. [1] is called “Type A” flapping motion. It is analyzed and an investigation is performed to assess the importance of the shape and thickness of the 2D wing profile on the aerodynamic force coefficients and vortex formation mechanisms at low Reynolds number (Re=1000). The sinusoidal flapping motion defined by Wang et al. [3] is called the “Type B” flapping motion. It is applied to an ellipse having 12% thickness and 0.01m chord length. The computed results are then compared with three dimensional experiments and empirical data [3]. Finally, the flapping motion defined by Freymuth [4] is called the “Type C” flapping motion is used. It is implemented to an elliptic wing model having a thickness of 1.6mm and a chord length of 0.0254m as in Freymuth’s experiments [4].

Generally, the motion of the flapping wing consists of three main phases: pitching down, rotation and translation. The translational phase consists of two half strokes-downstroke and upstroke (see Figure 3.2). The downstroke refers to the motion of the wing from its rearmost position (relative to the body) to its foremost position. The upstroke describes the return cycle. At either end of the half stroke, the rotational phases come into play, stroke reversal occurs, whereby the wing rotates rapidly and reverses its direction of motion for the subsequent half-stroke. During this process, the morphological lower surface becomes the upper surface and the leading edge always leads [19].

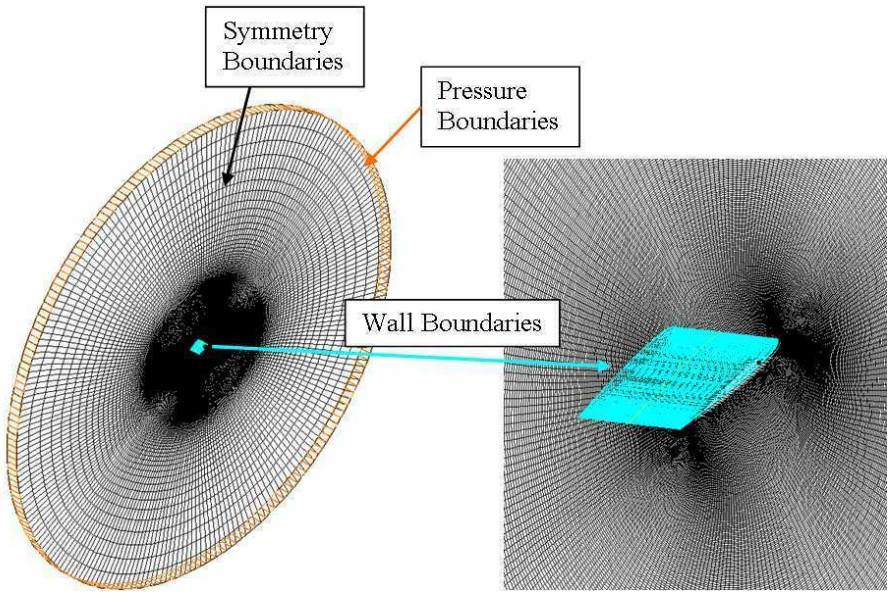

Figure 3.1 Boundaries location on the grid domain.

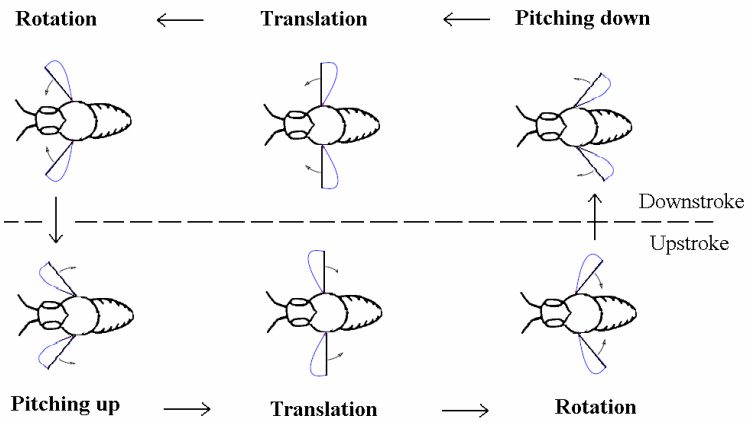

Figure 3.2 Half-strokes during an insect flapping cycle. The leading edge (thick line) always leads.

3.3.1 Investigation of Wing Model Kinematics of Type A

In this part of the study, the motion prescribed by Kurtuluş et al. [1] is implemented to the wing models. The wing models are SD 7003 airfoil profile, NACA 0012, NACA 0009 symmetric airfoil profiles and ellipses having 1%, 9% and 12% thickness all having 0.01m chord length. Center of rotation is at 50% chord location and in some cases it is changed to 25% chord (see Figure 3.3). The flow regime is assumed to be laminar, incompressible, and calculations are performed at low Re (Re=1000) number regime. For the present problem, the computations are performed at zero free-stream velocity in hover mode.

Grid domain used in the numerical part of the present study is formed via GRIDGEN V15, a package programmed to generate grid domain. O-type grid domain is used around the profiles. According to the results of grid refinement study, 229x340 (229 number of nodes around the profile) grid domain is used in the numerical simulation of this part (Figure 3.4).

The domains are formed in two sub-domains, inner domain is finer. The radius of the whole domain is 20 chords having a total of 77292 cells.

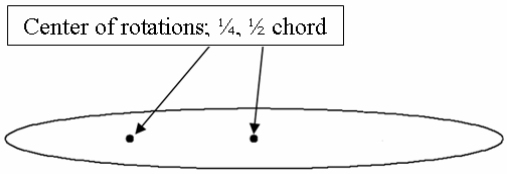

Figure 3.3 Ellipse having 12% c thickness profile and center of rotation points.

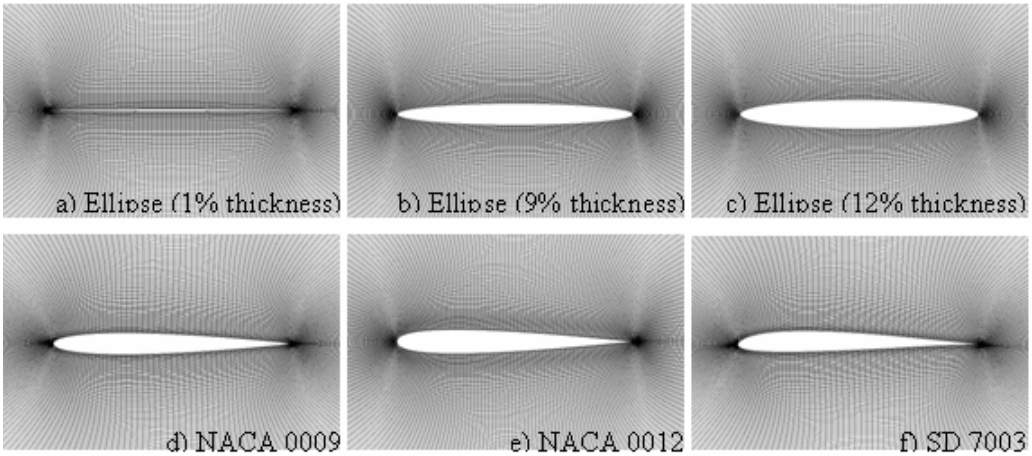

Figure 3.4 Inner grid domain of different wing profiles.

While in normal hovering flight, the wing motion during the upstroke is identical to that during the downstroke; in forward flight, the downstroke lasts longer than the upstroke because of the need to generate thrust [19]. In this study, although normal hovering mode is analyzed, both symmetric and cambered profiles are analyzed to see the difference.

Type A flapping motion description is represented schematically in Figure 3.5 in detail. Upstroke is represented by solid lines, and downstroke is represented by dashed lines in Figure 3.5. The profile starts its motion in the middle of the stroke (at x=0 and moves towards –x direction). Therefore, in the first region of the motion, the profile translates with a constant velocity and angle of attack until it reaches position $-x_a$ (angle of attack changing point) in the corresponding time interval (t_a). Then it starts to pitch up still with a constant velocity until point $-x_v$. The time corresponding to location-x_v is t_v. After location-$x_{v,}$ the profile starts to decelerate with an increasing

angle of attack and rotates around its center of rotation until it reaches 90^o angle of attack. In this way, it completes one quarter of the motion and reaches location $-x_{T/4}$. At this location the velocity of the profile becomes zero. The time corresponding the motion up to this location ($-x_{T/4}$) is T/4 where T is the total period of one complete cycle of the motion. After this location, the profile starts to accelerate with a decreasing angle of attack up to the location $-x_v$. After passing the location $-x_v$, the profile moves with a constant velocity but still decreasing angle of attack up to location $-x_a$. Until x=0, the profile translates with a constant velocity and angle of attack. In this way, the profile has completed one half of the motion cycle when it returns to the initial position of x=0. Second half of the motion is a mirror image of the first one. The rotation is such that the leading edge stays always as the leading edge during all phases of the motion.

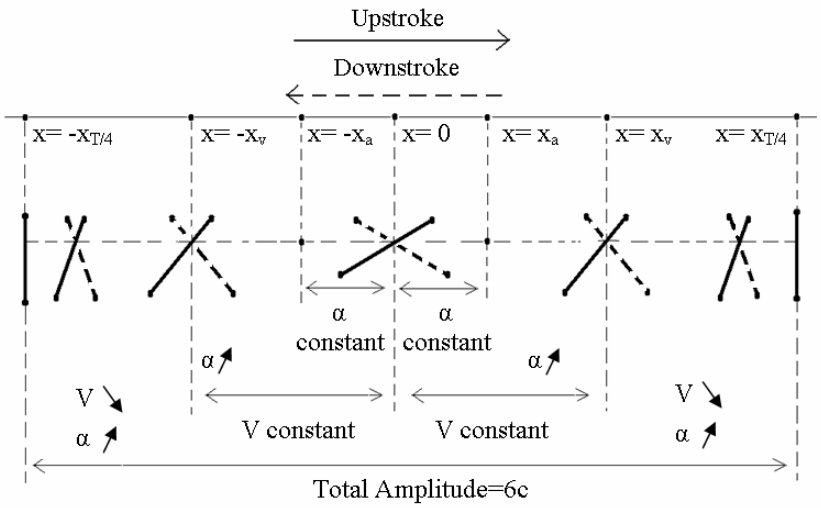

Figure 3.5 Schematic representation of flapping motion. Solid lines (—) represents upstroke, dashed lines (– –) represents downstroke of the profile.

The velocity V and the angular velocity variation ω are given in Eq. 3.5 and Eq. 3.6, respectively. Kurtulus et al. [1] have chosen this type of motion to ensure the continuity of velocities and the accelerations between the two phases of translational motion.

$$V = V_0 \cos\left(\frac{\pi}{2}\frac{t - t_v}{\frac{T}{4} - t_v}\right) \tag{3.5}$$

$$\omega = -\frac{\omega_{\max}}{2}\left(1 - \cos\left(\frac{\pi(t - t_a)}{\frac{T}{4} - t_a}\right)\right) \tag{3.6}$$

where

$$\omega_{\max} = \frac{2\alpha_0}{\frac{T}{4} - t_a} \tag{3.7}$$

$$T = \frac{4\pi}{2|V_0|}(x_{T/4} - x_v) + t_v \tag{3.8}$$

For the computation of the aerodynamic forces, the total forces are calculated as the sum of the shear force and the pressure force on the wall [1].

$$\vec{F}_t = \vec{F}_s + \vec{F}_p \tag{3.9}$$

The shear force is:

$$\vec{F}_s = -\tau_w A_b \frac{\vec{v}_{par}}{|\vec{v}_{par}|} \tag{3.10}$$

where A_b is the elementary wall area and $\vec{v}_{par}$ is the velocity vector component parallel to the wall and τ_w is the wall shear stress.

The pressure force coefficient is given by the Equation 3.11.

$$\vec{F}_p = p_b A_b \vec{n}_b \tag{3.11}$$

where p_b is the pressure on the elementary wall area A_b and $\vec{n}_b$ is the outward pointing unit area vector.

Mean aerodynamic coefficients are calculated as the time average of instantaneous values throughout one period (Eqs. 3.12-3.13). Mean aerodynamic coefficients are calculated for the 7th period of the motion to avoid the effect of impulsively starting.

$$\overline{C}_L = \frac{1}{T}\int_{t=6T}^{t=7T} C_L(t)dt \tag{3.12}$$

$$\overline{C}_D = \frac{1}{T}\int_{t=6T}^{t=7T} C_D(t)dt \tag{3.13}$$

3.3.2 Investigation of Wing Model Kinematics of Type B

For the simulation of flapping kinematics of Wang et al. [3], an ellipse of 12% chord thickness is used (c=0.01m). For the ellipse (e=12%c), the same grid domain is used as the previous study. The wing follows a sinusoidal flapping and pitching motion (Eqs. 3.14-3.15, respectively) [3]. Specifically, the wing sweeps in the horizontal plane and pitches about its spanwise axis with a single frequency *f*:

$$x(t) = \frac{A_0}{2}\cos(2\pi ft) \tag{3.14}$$

$$\alpha(t) = \alpha_0 + \beta\sin(2\pi ft + \phi) \tag{3.15}$$

where *x(t)* is the position of the center of the wing, and α(t) is the wing orientation with respect to the x-axis. By definition, the translational and angular velocities are given by $U_0(t)=dx(t)/dt$ and $\Omega(t)=d\alpha(t)/dt$. The parameters include the stroke

amplitude A_0, the initial angle of attack α_0, the amplitude of pitching angle of attack β, the frequency f and the phase difference ϕ between $x(t)$ and $\alpha(t)$.

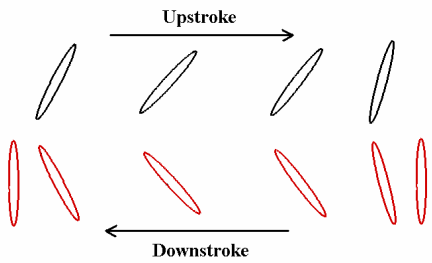

Figure 3.6 Sinusoidal motion of the profile during one stroke.

The translational motion of the wing is completely specified by two dimensionless parameters, Reynolds number, $Re=U_{max}c/\nu=\pi fA_0c/\nu$, and A_0/c, where U_{max} is the maximum flapping velocity, and c is the chord length. From their steady-state 2D numerical data Wang et al. [3] found the approximated empirical correlations for both of the aerodynamic coefficients, namely, C_L (Eq. 3.16) and C_D (Eq. 3.17) in terms of angle of attack α.

$$C_L = 1.2\sin(2\alpha) \tag{3.16}$$

$$C_D = 1.4 - \cos(2\alpha) \tag{3.17}$$

The constants depend on the Reynolds number, details of the wing, etc. They implemented this empirical data (Eq. 3.16-Eq. 3.17) for all of the instantaneous angle of attack variations that they have investigated. For each α value, C_L and C_D values are calculated. Quasi-steady translational lift (L_T) and drag forces (D_T) are calculated, $0.5\rho u^2 C_L$ and $0.5\rho u^2 C_D$, respectively. All of the numerical and empirical forces are normalized by the maxima of the corresponding to quasi-steady forces as described in the study of Wang et al. [3].

3.3.3 Investigation of Wing Model Kinematics of Type C

In this part of the study, the flapping motion as defined by Freymuth [4] is investigated. Freymuth [4] used a planar airfoil having a thickness of 1.6mm and a chord of c=2.54cm with rounded edges to execute the combined plunging and pitching motions in the experiments. In the present numerical investigations an elliptical wing having the same thickness and chord as Freymuth's model is used.

The grid domain used for the simulations of the Freymuth [4] motion kinematics is generated by carrying out the same procedure used in Type A and Type B motion solutions. 259 numbers of nodes are put on the profile. The radius of the whole domain is 20 chords having 82560 cells. The computational grid domain used in this part is presented in Figure 3.7.

The airfoil performs a translating (plunging) motion [4] h in horizontal direction (Eq. 3.18):

$$h = h_a \sin(2\pi f t) \tag{3.18}$$

where h_a is the amplitude of linear translation, f is the frequency of sinusoidal oscillation and t is the time. Considering that the airfoil performs a pitching motion (Eq. 3.19) simultaneously, around its half chord axis:

$$\alpha = \alpha_0 + \alpha_a \sin(2\pi f t + \phi) \tag{3.19}$$

where α is the pitch angle with respect to the horizontal as shown in Figure 3.8, α_0 is the mean pitch angle, α_a is the pitch amplitude and ϕ is the phase difference between pitching and plunging.

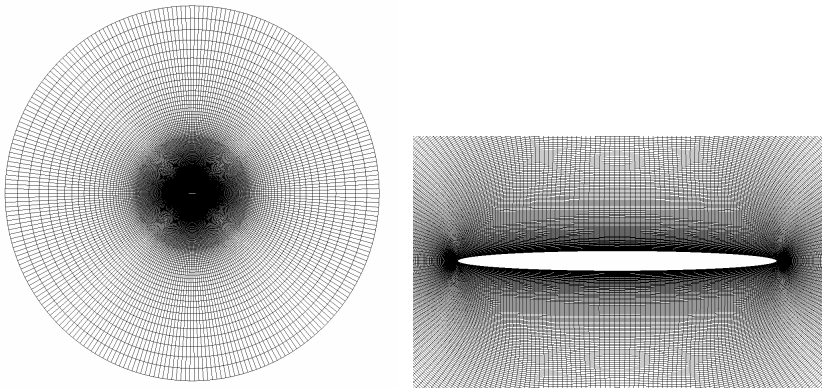

Figure 3.7 Computational Grid Domain used in Type C.

Dimensionless parameters of the system are: α_0, α_a, ϕ, the dimensionless plunge amplitude h_a/c and a Reynolds number;

$$R_f = 2\pi f h_a c / \nu \tag{3.20}$$

based on the maximum plunge speed $2\pi f h_a$ and on c, where ν is the kinematic viscosity.

Two simple modes of hovering were initially identified by Freymuth [4]: “Mode 1” or “water treading mode” is characterized by $\alpha_0=0^o$ and $\phi=90^o$ and is sketched in Figure 3.8. The airfoil starts a cycle from the position of having pitch amplitude (α_a) at middle of the downstroke (indicated as right arrow). It moves a distance $2h_a$ to the right to reach its initial position. The right edge of the airfoil is leading during its motion to the right but when the airfoil returns left, the leading and trailing edges switch their roles.

“Mode 2” or “degenerate figure eight mode” or “normal hovering mode” is sketched in Figure 3.9 and is characterized by $\alpha_0=90^o$. In this mode leading, and trailing edges do not switch role during one cycle. Leading edge always leads. This mode resembles the hovering of hummingbirds and most flying insects [4].

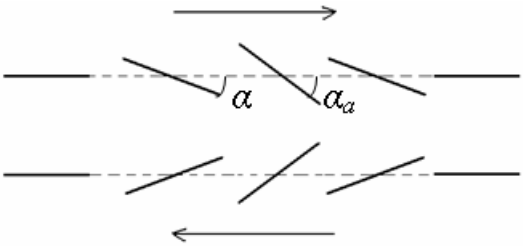

Figure 3.8 Sketch of combined translating-pitching motions of the airfoil for one cycle of mode 1 hovering ($\alpha_0=0^o$, $\phi=90^o$).

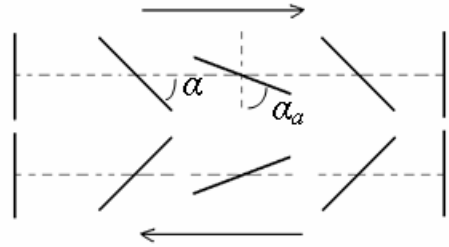

Figure 3.9 Sketch of combined translating-pitching motions of the airfoil for one cycle of mode 2 hovering ($\alpha_0=90^o$, $\phi=-90^o$).

To characterize the time averaged thrust T on the airfoil, a thrust coefficient C_T is defined in Reference [4] (Eq. 3.21):

$$C_T = \frac{T}{0.5\rho\overline{V_t^2}cl} \tag{3.21}$$

where ρ is the air density, l>>c, is the span of the airfoil and

$$\overline{V_t^2} = 0.5(2\pi f h_a)^2 \tag{3.22}$$

is the mean square speed of the horizontal airfoil motion (Eq. 3.23). From the momentum theorem

$$T = \rho l \int_{-\infty}^{\infty} \overline{V^2} dx \tag{3.23}$$

where $\overline{V^2}$ is the mean square velocity at a sufficient distance from the airfoil. The thrust coefficient is found as follows (Eq. 3.24);

$$C_T = \int_{-\infty}^{\infty} \overline{V^2} dx / (\pi f h_a)^2 c \tag{3.24}$$

Since thrust during actual hovering would be upward C_T may also be considered as a lift coefficient of the hovering airfoil [4].

3.4 Computational Grid Domain

A grid refinement study was carried out by using NACA 0012 airfoil and ellipse having 12% thick profiles. Flapping motion prescribed by Kurtulus et al. [1] is used at Reynolds number Re=1000, x_v=2c and x_a=2c, center of rotation a=0.25c and angle of attack $\alpha=45^o$. O-type grid domain is used around the profiles. The grid domains are 175x198 (175 points around the profile), 229x340 (229 points around the profile) and 260x340 (260 points around the profile). The C_L distributions of these three grid domains are presented in Figure 3.10. To decide which grid domain should be used in the numerical analysis of the problem, vorticity contours of the profiles at some indicated times are also compared (see Figure 3.11 and Figure 3.12). According to C_L distributions there are no big difference between 229x340 and 260x340 grid domains for both NACA 0012 and Ellipse (e=12%). However, this is not sufficient to decide on the grid domain. As it is known, vortex shedding mechanism has an important role while flapping motion is investigated. Although there is a small difference in capturing the vorticity trace of the motion between 229x340 and 260x340 grid domains, it is not a big difference when the CPU times are considered (see Figure 3.13). In Figure 3.13, CPU time spent for 5000 iterations is represented for three different grid domains. Therefore, it is decided that the 229x340 grid domain is sufficiently fine for DNS solution of the problem. Clusters used in this present study are Albatros N. These clusters have 2.4 GHz. CPU, 1.0 Gb RAM, and Xeon processor.

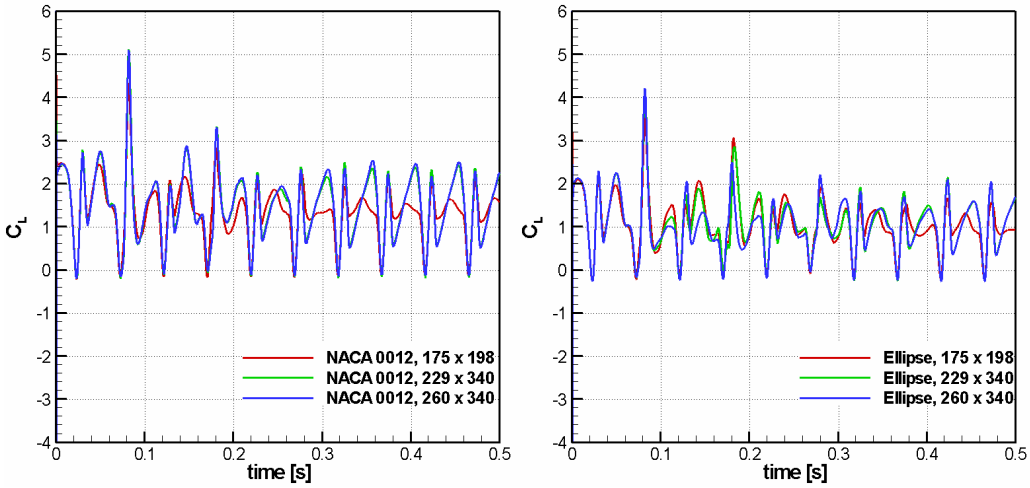

Figure 3.10 Lift Coefficient (C_L) of different grid domains for NACA 0012 and Ellipse (e=12%) profiles.

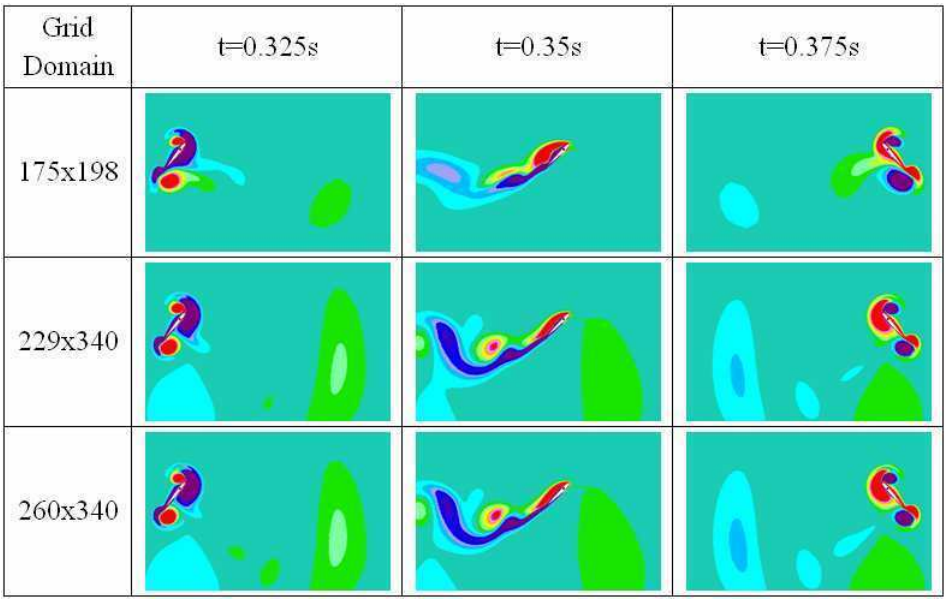

Figure 3.11 Vorticity contours of three different grid domains for NACA 0012 at indicated times.

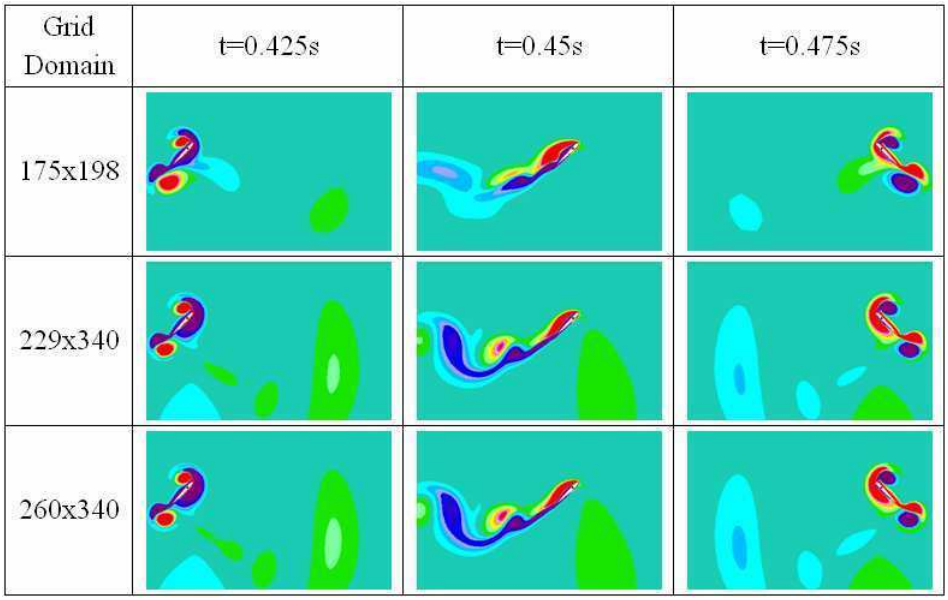

Figure 3.11 (Cont'd) Vorticity contours of three different grid domains for NACA 0012 at indicated times.

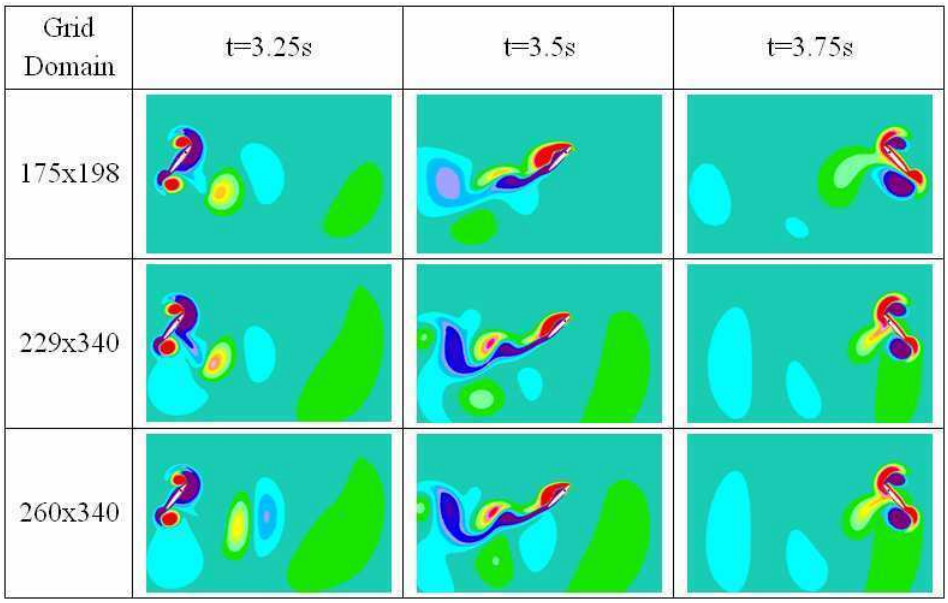

Figure 3.12 Vorticity contours of three different grid domains for Ellipse (e=12%) at indicated times.

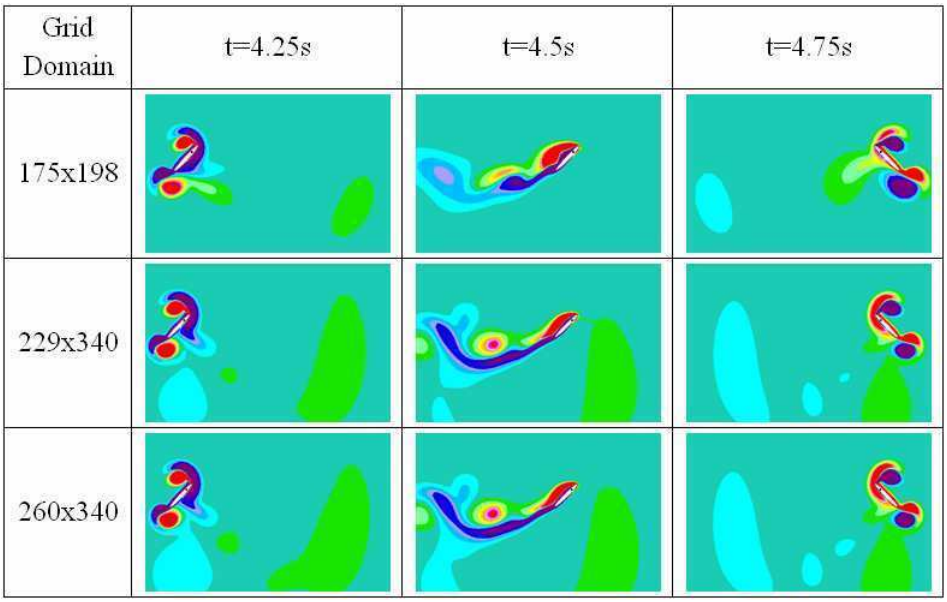

Figure 3.12 (Cont'd) Vorticity contours of three different grid domains for Ellipse (e=12%) at indicated times.

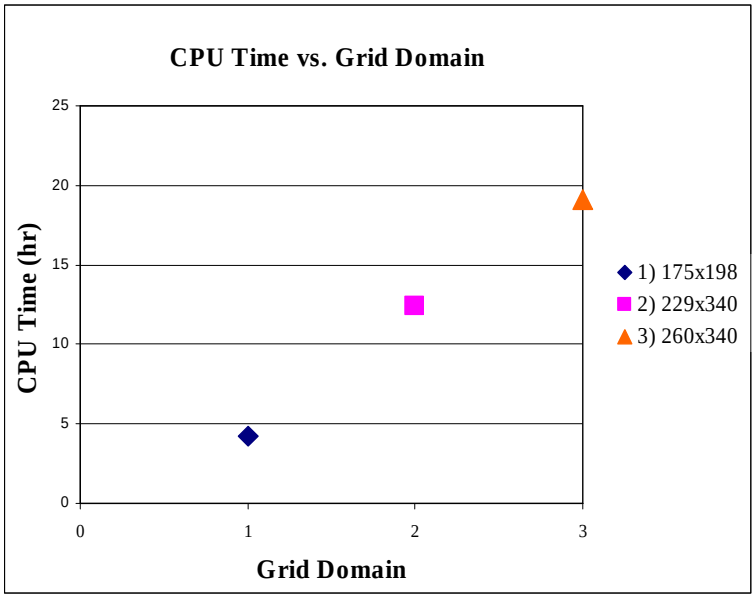

Figure 3.13 CPU Time vs. Grid Domain

CHAPTER IV

NUMERICAL RESULTS

This chapter is devoted to the numerical analysis of different flapping motion kinematics for different Reynolds numbers in the range of (10^1-10^3). Effects of some parameters on the aerodynamic forces and the vortex shedding mechanisms are investigated.

The numerical solution technique defined in Chapter II is applied to three different flapping kinematics. The first kinematics, designated as type A, is characterized by Kurtuluş et al. [1]. The second one, designated as Type B, is the one proposed by Wang et al. [3] and the third one, Type C, is the one suggested by Freymuth [4].

An investigation is performed to understand the effects of profile shape and thickness on the aerodynamic force coefficients and vortex shedding mechanism by using the flapping motion defined by Kurtuluş et al. [1]. The effects of Reynolds number and stroke amplitude on the aerodynamic force coefficients are investigated by using the study of Wang et al. [3]. Finally, the study of Freymuth [4] is analyzed and experimental lift coefficient data and vortex formation is compared with the presented computed results.

4.1 Parametrical Study on Unsteady Aerodynamics of Different Wing Profiles at Low Reynolds Number by using Type A Flapping Motion

In this part of the study, Type A flapping motion defined in Chapter III is implemented to the computations. To analyze the effects of profile shape and thickness, two dimensional elliptic wing profiles with varying thicknesses (e=1%,

e=9% and e=12%) are compared with NACA (namely NACA 0009 and NACA 0012) and SD 7003 airfoil profiles all having the same chord length, (0.01m) [2].

The instantaneous angle of attack and velocity distributions are represented in Figure 4.1. The different parameters studied are summarized in Table 4.1.

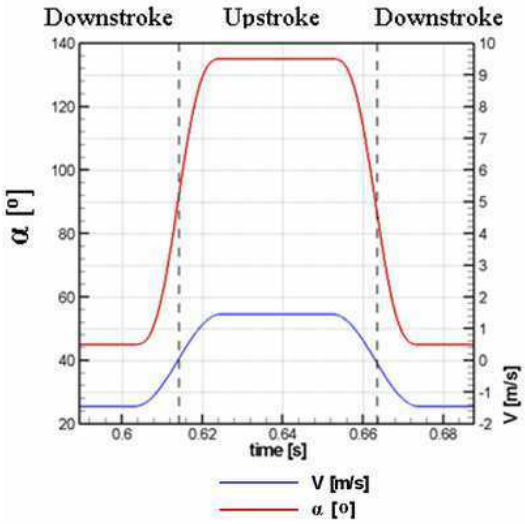

Figure 4.1 Instantaneous velocity and angle of attack distributions of the flapping motion.

Table 4.1 Different profiles and parameters investigated for Re=1000, x_v=2c, x_a=2c case

	Initial angle of attack, α_0	**center of rotation, *a***
Ellipse (9% thickness)	30°, 45°, 60°	c/4,c/2
Ellipse (12% thickness)	30°, 45°, 60°	c/4, c/2
Ellipse (1% thickness)	30°, 45°, 60°	c/4, c/2
NACA 0009	30°, 45°, 60°	c/4, c/2
NACA 0012	30°, 45°, 60°	c/4, c/2
SD 7003	30°, 45°, 60°	c/4, c/2

4.1.1 Evolution of Instantaneous Flow for Different Profiles

As a consequence of the kinematics of the flapping motion, due to unsteady separation and coherent vortex shedding, the aerodynamic loads exhibit a highly unsteady behavior. Lift coefficient (C_L) and drag coefficient (C_D) are calculated instantaneously during the 7th period of the flapping motion and represented in Figure 4.2 for elliptical profile with 12% thickness. The results are compared for different α_0 values with the center of rotation located at the half-chord position (a=c/2). It is observed that for α_0=30° case, the lift coefficient increases gradually from the beginning of the upstroke where it reaches a peak value at the end of the translational phase of the upstroke. Moreover, it is noted that the C_L is close to zero at the beginning of the upstroke for this case. However, for higher angles of attack, namely 45° and 60°, the peaks at the beginning of the upstroke are relatively important. The maximum peaks of the drag coefficients occur at the beginning of the upstroke for all three cases. By comparing different angles, it is observed that C_L reaches its minimum value for α_0 =45° case (C_L=-0.294) at t=0.612s and it reaches its maximum value (C_L=2.10) at t=0.625s for α_0 =60^o case. C_D reaches its absolute maximum value ($|C_D|$=3.27) during upstroke at t=0.624 s for 60^o initial angle of attack.

The instantaneous vorticity contours of the same profile are represented in Figure 4.3 for these three different starting angles of attack from the beginning to the end of the upstroke. At the beginning of the upstroke the lift coefficients for all of the cases are zero, but the highest drag coefficient (the force in the x direction) has a maximum value for 30° case just at the beginning of the upstroke. This peak value decays in time as the starting angle of attack increases.

Just at the beginning of the upstroke the vortex shedding are observed to be different for different α_0 values. The traces of the vortices from the previous downstroke are very strong for α_0=60° case. The counter-clockwise (red) trailing edge vortex is increasing in magnitude for high α_0 values and detaches from the airfoil surface

during previous downstroke (t=0.615s in Figure 4.3). The profile starts to accelerate at the beginning of the upstroke and reaches $V(t)=0.075V_0$ value at t=0.615s with an angle of attack of $\alpha(t)$= 84.2°, 85.7° and 87.1° for α_0=30°,45° and 60° cases respectively. There is also a counter-clockwise leading edge vortex which is just generated at the beginning of the upstroke which pushes and deforms the clockwise vortex dominant at the lower surface of the airfoil. At t=0.619s, lift and drag coefficients are very close to zero (C_L= -0.164 and C_D= 0.062) for α_0=30°. At this instant, the lift coefficient is higher for 45° case compared to other angles and the drag coefficient has a similar order of magnitude compared with α_0=60° (C_L= 1.908 and C_D= -2.57 for α_0=45° and C_L= 1.166 and C_D= -2.65 for α_0=60°). The ellipse is moving with a velocity of $V(t)=0.71V_0$ and its angle of attack is $\alpha(t)$= 40.7°, 53.1° and 65.4° for α_0=30°, 45° and 60° cases respectively. Until t=0.625, according to the kinematics of the motion, the velocity of the profile increases to $V=V_0$ and its angle of attack decreases to α_0 value.

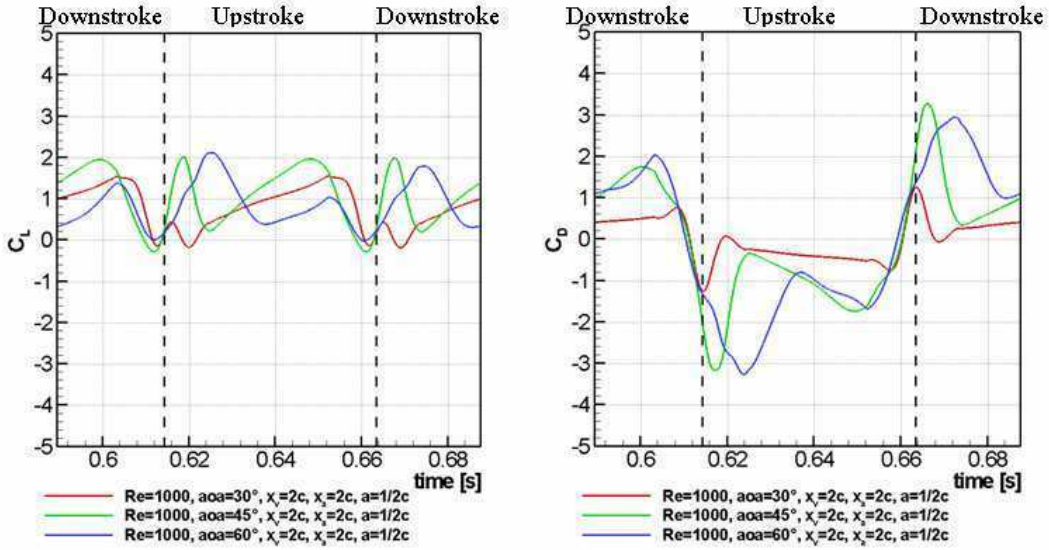

Figure 4.2 C_L and C_D distributions of ellipse (e=12%c) for different angles of attack with center of rotation at a=c/2.

For α_0=30° case, at t=0.629s, the leading edge vortex on the upper surface of the airfoil stays attached to the ellipse. However, for 45° case the same leading edge

vortex detaches completely from the upper surface of the ellipse leaving its trace at the mid of the domain. For 60° case, at t=0.629s, although the same leading edge vortex detaches from the upper surface of the ellipse, it stays attached to the airfoil leading edge until t=0.639s until a clockwise vortex (blue) is formed on the mid-upper surface of the airfoil. The airfoil enters into the trace of the clockwise leading edge vortex (blue) for 60° case at t=0.629s by pushing downwards the trace of the counter-clockwise trailing edge vortex (red) generated during the previous downstroke. The lift coefficients at t=0.629s for 30° and 45° cases are very close to each other (C_L= 0.617 for α_0=30° and C_L= 0.614 for α_0=45°). However, C_L of 60° at this instant is twice of these cases (C_L=1.575 for α_0=60°). The drag coefficients are also increasing with increasing α_0 values at the same time instant with a highest value of -2.3 for α_0=60°.

At t=0.639s, the profile is approximately at mid-amplitude location of the flapping domain. The trailing edge vortex is very dominant for high angles of attack. The trailing and leading edge vortices are behaving relatively different for different α_0 values. The traces of both of these vortices are observable until the end of the stroke without any detachment for 30° case. At this time, the C_L values corresponding to different α_0 values are given as C_L= 0.994 for α_0=30°, C_L= 1.387 for α_0=45° and C_L= 0.383 for α_0=60°. Corresponding drag coefficients are found to be as C_D=-0.404 for α_0=30°, C_D= -0.996 for α_0=45° and C_D= -0.860 for α_0=60°. The highest lift and drag occurs at 45° angle of attack. The lift coefficient is smallest for 60° angle of attack where two counter-rotating vortices exist on the upper surface of the airfoil. This vortex formation at 60° is also represented step by step in the following section for NACA0012 where the formations of the vortices are very similar for Re=1000.

The constant velocity translational phase finishes at t=0.652s and after this time the airfoil starts to accelerate once more by increasing its angle of attack. It is observed that at t=0.656s another leading edge vortex grows and forces the previous one to detach from the ellipse's upper surface for α_0=60° case. Locally, these two leading edge vortices and trailing edge vortex form a similar pattern to Kármán vortex street.

The velocity attains a value of $V(t)=0.84V_0$ with changing angles of attack of $\alpha(t)=$ 34.5°, 48.4° and 62.3° corresponding to $\alpha_0=30°$, 45° and 60° cases respectively. At this instant, $C_L=1.43$ for $\alpha_0=30°$, $C_L= 0.554$ for $\alpha_0=45°$ and $C_L= 0.636$ for $\alpha_0=60°$. In the mean time, $C_D= -0.683$ for $\alpha_0=30°$, $C_D= -0.96$ for $\alpha_0=45°$ and $C_D= -1.09$ for $\alpha_0=60°$. As a result, at t=0.656s, the lift coefficient has its maximum value for $\alpha_0=30°$ angle of attack case which is more than twice of the value attained at $\alpha_0=45°$ and the lift coefficient is the lowest when compared to other angles. However the drag coefficient is increasing with the angle of attack where its lowest value is obtained at $\alpha_0=30°$ case and its highest value at $\alpha_0=60°$.

Close-up sequence of instantaneous vorticity contours and C_L distributions of ellipse (e=12%c) at some instances are presented in from Figure 4.4 to Figure 4.7 for the same case as analyzed in Figure 4.2. Close-up views and C_L distributions helped to investigate in detail the vortex formations. Different vortex topologies are observed for different α_0 values. Both trailing edge vortex and leading edge vortices are very strong, grow very and detach quickly from the airfoil surface for high α_0 values. The angle of attack, velocity, C_L, and C_D values at the indicated time instances are noted on the views (see Figure 4.4-Figure 4.7).

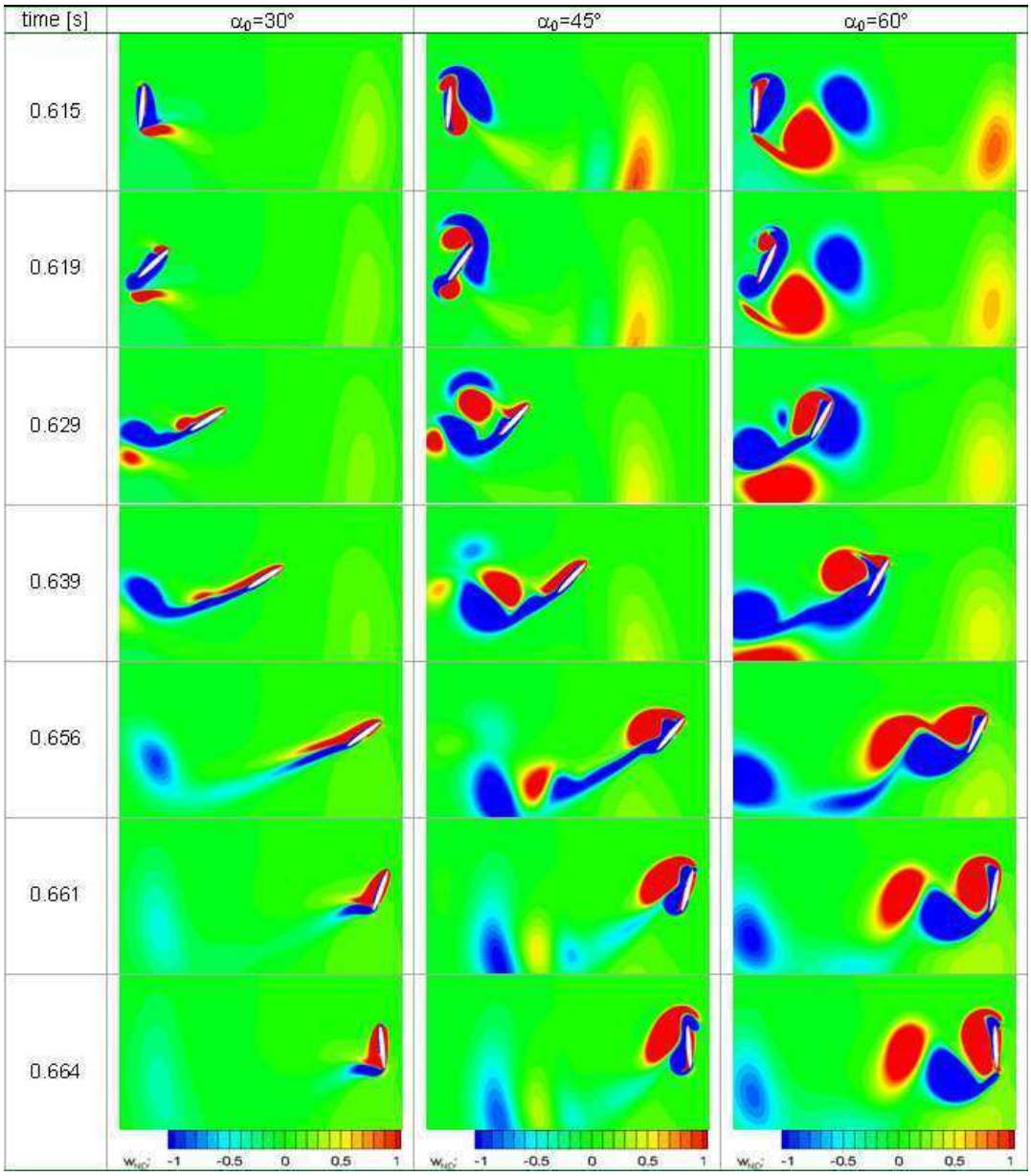

Figure 4.3 Instantaneous vorticity contours of ellipse (e=12%c) for different α_0 with a=c/2.

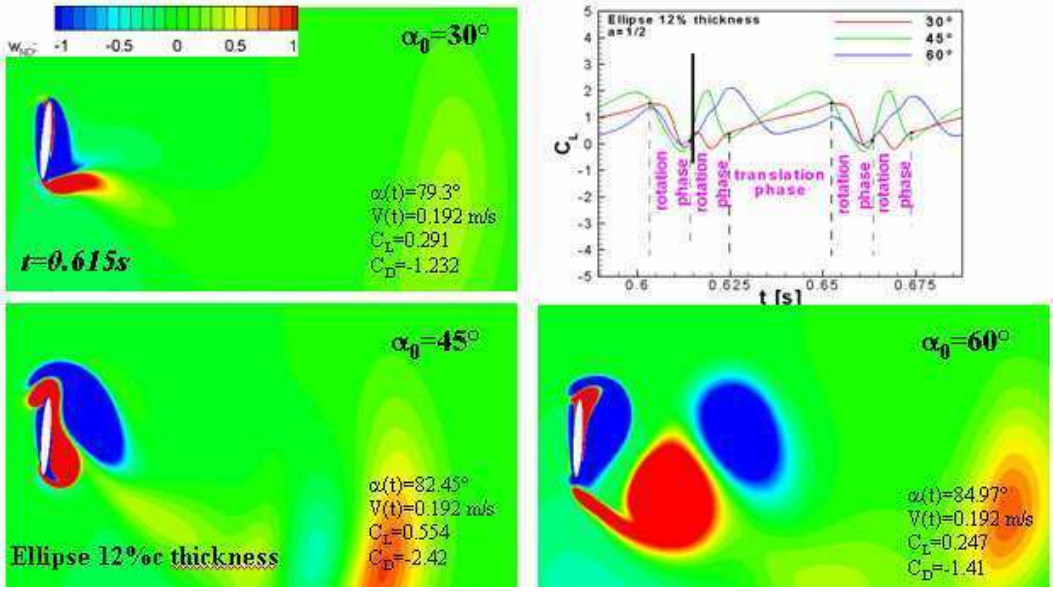

Figure 4.4 Close-up view of instantaneous vorticity and C_L distributions at t=0.615s, a=c/2.

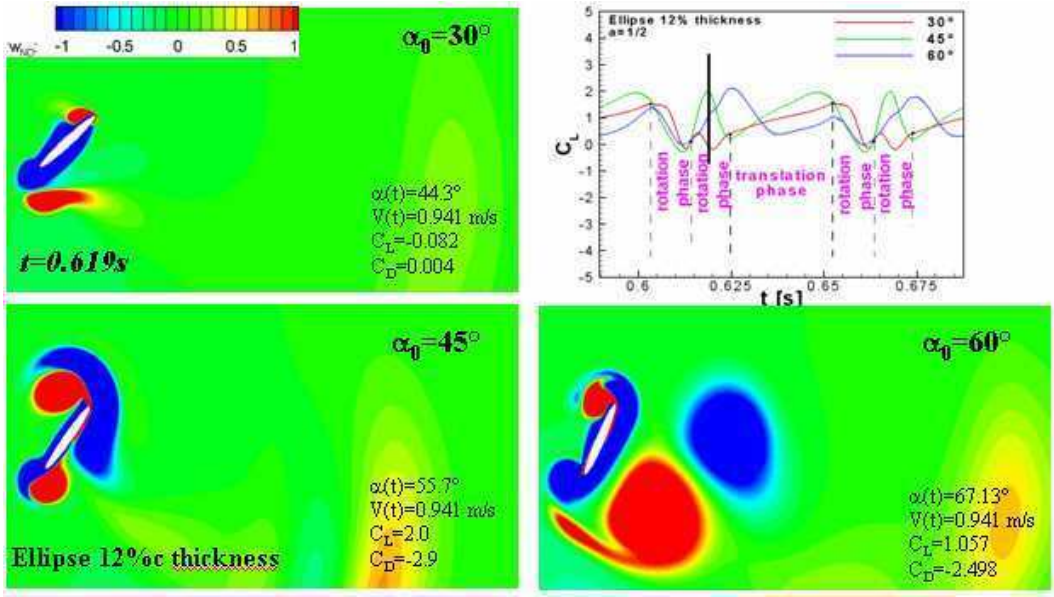

Figure 4.5 Close-up view of instantaneous vorticity and C_L distributions at t=0.619s, a=c/2.

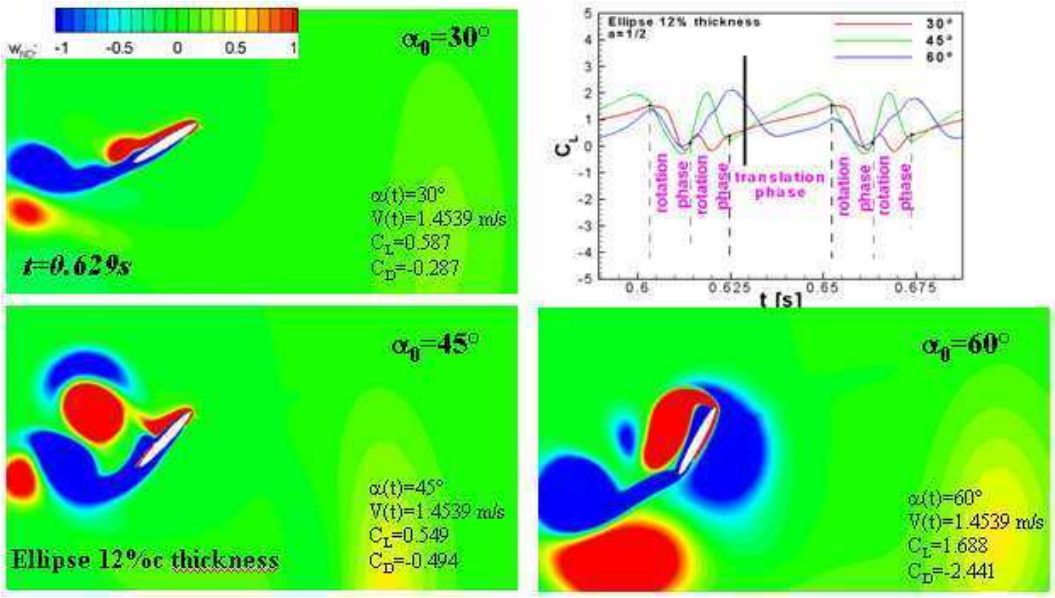

Figure 4.6 Close-up view of instantaneous vorticity and C_L distributions at t=0.629s, a=c/2.

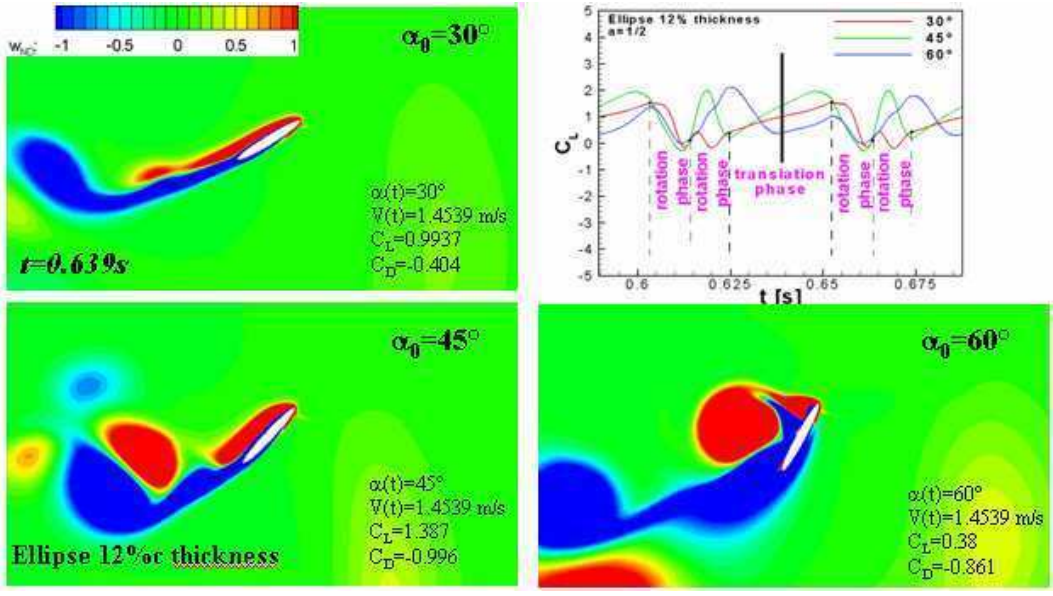

Figure 4.7 Close-up view of instantaneous vorticity and C_L distributions at t=0.639s, a=c/2.

Instantaneous lift and drag coefficients are obtained during the 7th period of the flapping motion for three different thickness ratio ellipses (e=1%, 9% and 12%), two different thickness NACA profiles (NACA 0012 and NACA 0009) and one SD 7003

airfoil profiles for three different angles. The results are given in Figure 4.8 for 45° angle of attack with their centers of rotation located at c/4.

The force coefficients of different thickness (e=9% and e=12%) ellipses are observed to have almost the same functional dependence on the angle of attack but with different magnitudes [33]. The lift comes from viscous forces [3], especially at this low Re number regime. NACA profiles give higher force coefficients at the peak locations. It is also noted that the aerodynamic coefficients of thinner profiles (especially ellipse) are slightly higher in magnitude than their thicker cases. The same behavior is also observed for other angles of attacks.

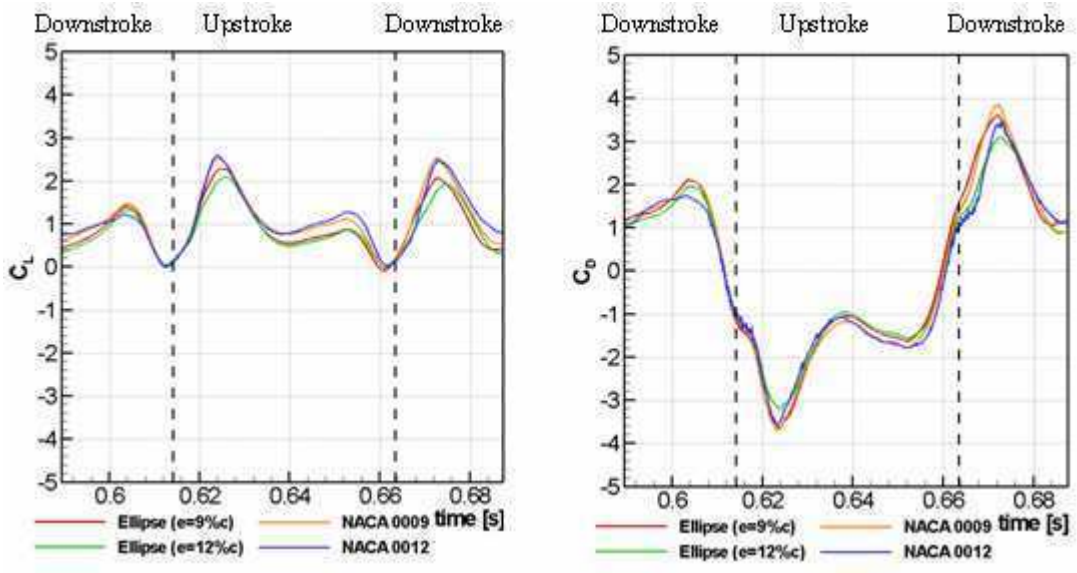

Figure 4.8 C_L and C_D distributions of profiles for $\alpha_0=45^o$, a=c/4.

Instantaneous vorticity contours of different profiles (ellipse (e=9%), NACA 0009, NACA 0012) as investigated in Figure 4.8 are also represented in Figure 4.9. The thickness effects on the vorticity contours of the profiles are not very clearly distinguishable for the analyzed cases in view of the vortex shedding (see Figure 4.9).

The effect of profile thicknesses is very minor for e=9% and e=12% cases. However, the difference between the Ellipse 9%c and NACA profiles are observable. The formation of the counter-clockwise leading edge vortex at the beginning of the upstroke and its vorticity radius are different for ellipse and NACA profiles (t=0.619s). Although its influence is not clearly visible in C_L curves it is observable in C_D curves at the peak locations. At t=0.639s, during the pure translation, the clockwise (blue) trailing edge vortex starts to detach earlier from the lower surface of NACA 0012 than the others'. At t=0.656s, this trailing edge vortex completely breaks off the new trailing edge vortex of NACA profiles. In addition, the leading edge vortex detaches completely from the airfoil at this time and its trace is highly visible until the end of the upstroke (see Figure 4.9 at t=0.661s).

Instantaneous lift and drag coefficients obtained during the 7^{th} period of the flapping motion of the profiles for the case of $\alpha_0=60^o$, a=c/2 are represented in Figure 4.10. In this case evaluation, it is noticed that the Ellipse (e=1%c) and SD 7003 do not have effective C_L values at the peak locations as in the case of a=c/4 and $\alpha_0=45^o$.

However, ellipse (e=1%) has absolute maximum C_D values at the beginning of the translational phases of the upstroke ($|C_D| = 4.092$ at t=0.623s) and downstroke ($|C_D| = 4.030$ at t=0.672s).

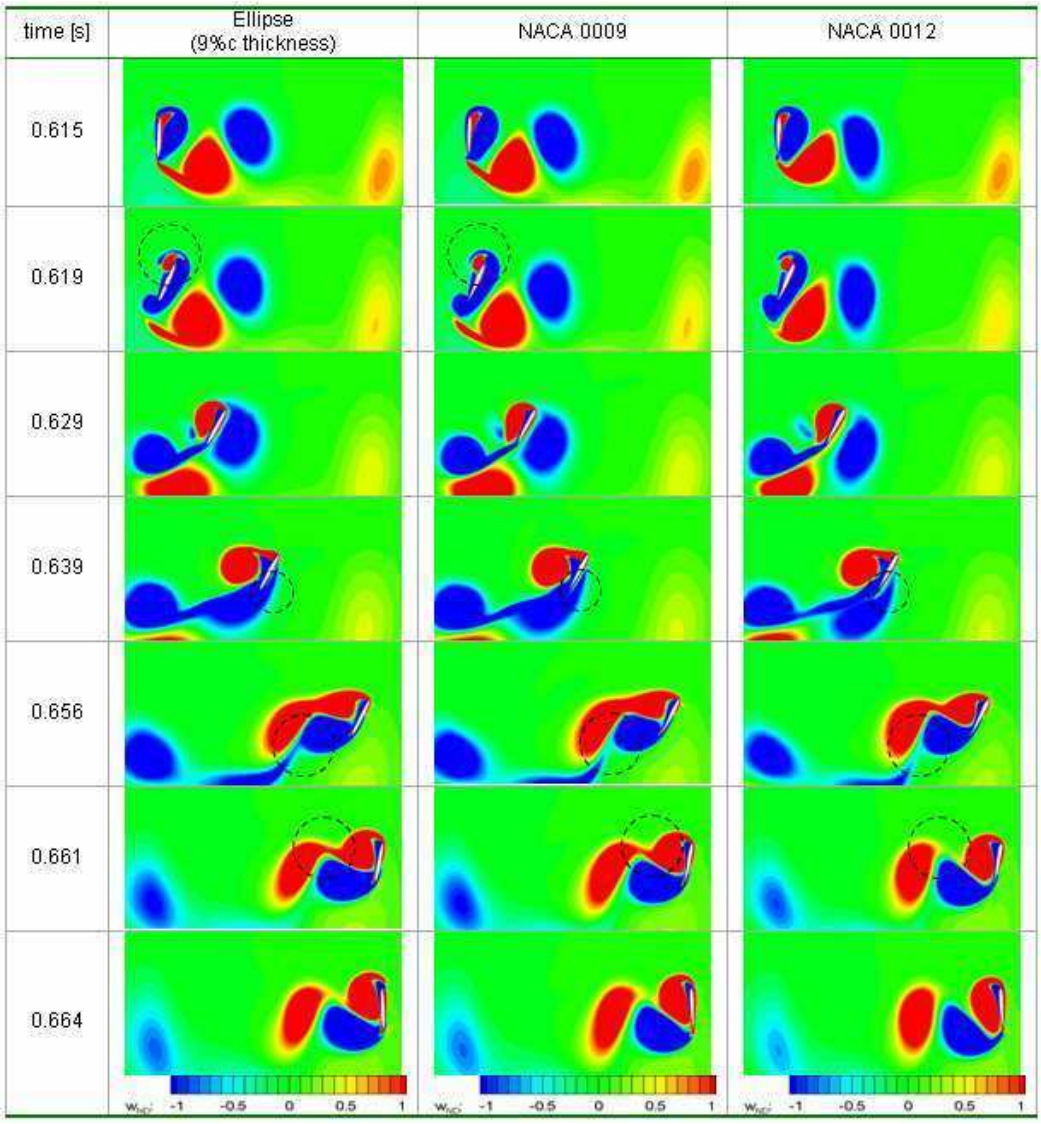

Figure 4.9 Instantaneous vorticity contours of profiles for $\alpha_0=60^o$, a=c/4.

To see the camber and thickness effects on the aerodynamic force coefficients and on vortex shedding mechanisms more clearly, the aerodynamic force coefficients (see Figure 4.11) and the instantaneous vorticity contours (see Figure 4.12) of different profiles (ellipse (e=1%c and e=12%c), and SD 7003) are also represented for the case of a=c/2 and $\alpha=60^o$, during the 7^{th} period of the flapping motion. The effect of thickness for the elliptic profiles (e=1%c and e=12%c) can be clearly observed at the peak locations. This result is expected as indicated in the literature [33].

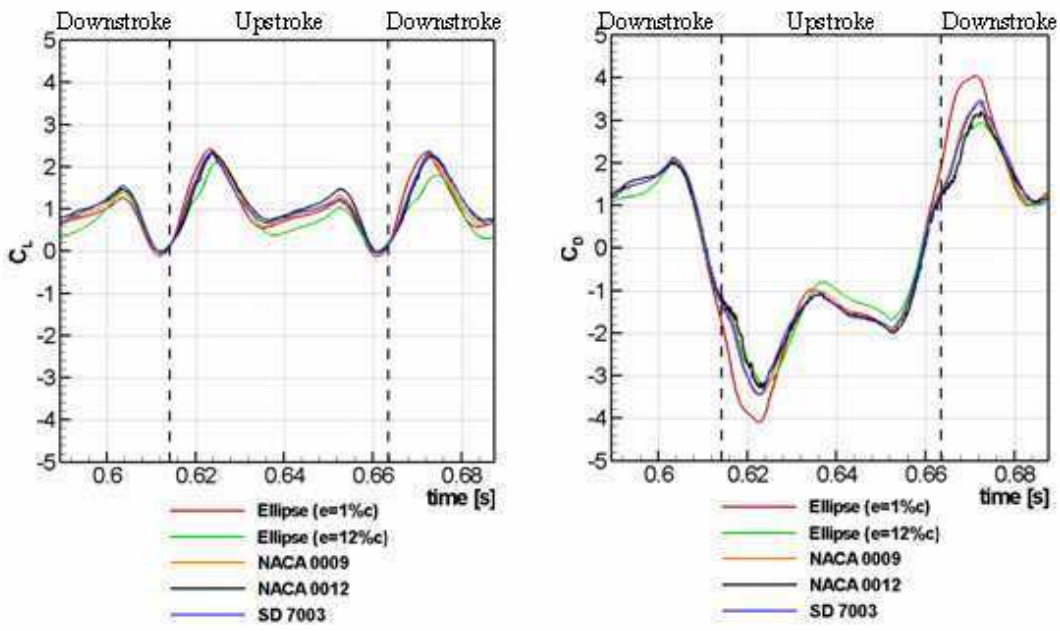

Figure 4.10 C_L and C_D distributions of the profiles for $\alpha_0=60^o$, a=c/2.

The mean aerodynamic force coefficients are calculated by using Eq. 3.12 and Eq. 3.13 and presented in Table 4.2 for the case of a=c/2, $\alpha=60^o$. Although the force coefficients of NACA 0012 do not have an effective value during one stroke of the motion, NACA 0012 has the maximum mean lift coefficient value.

Table 4.2 Mean aerodynamic coefficients of profiles for a=c/2, $\alpha=60^o$.

Profile	$\overline{C}_L$	$\overline{C}_D$
Ellipse (e=1%c)	0.984	0.0050
Ellipse (e=12%c)	0.831	0.0079
NACA 0009	1.019	0.0144
NACA 0012	1.082	-0.0103
SD 7003	1.052	0.0187

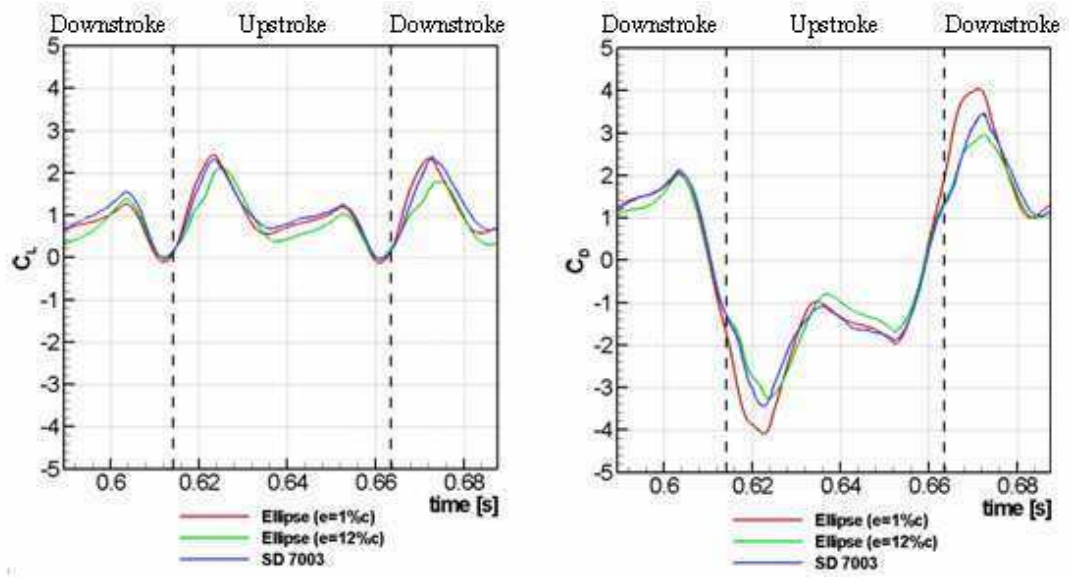

Figure 4.11 C_L and C_D distributions of Ellipse and SD 7003 profiles for $\alpha_0=60^o$, a=c/2.

The following explanations of vortex shedding are for Figure 4.12. The general, character of the vortex shedding obtained from different profiles is similar. However, at some regions small differences may result in effective peaks in force coefficients curves. The traces of the vortices left from the previous downstroke are very influential for all cases. The counter-clockwise (red) trailing edge vortex starts to detach earlier from the surface of thicker ellipse (e=12%c) than that of thinner ellipse (e=1%c) (at t=0.615s). The radius of the counter-clockwise leading edge vortex formed at t=0.615s and t=0.619s is different for ellipses and SD 7003. This difference is not clearly observable in C_L curves but observable in C_D curves at this instant (t=0.619s). At t=0.629s, the profiles enter to the trace of the clockwise leading edge vortex (blue) while pushing the trace of the counter-clockwise trailing edge vortex (red) generated during the dowstroke down. The counter-clockwise (red) leading edge vortex has started to detach from the leading edge of the profiles but it is observable in ellipse (e=1%c) case. The counter-clockwise (red) and clockwise (blue) vortices on the upper surface of SD 7003 and ellipse (e=12%c) profiles are adjacent to each other (t=0.629s). Clockwise vortex (blue) on the mid-upper surface of the profiles advances to cause the leading edge vortices to detach from the upper surface of the profiles (t=0.639s). This clockwise vortex on ellipse (e=12%c) is

stronger than on ellipse (e=1%c) and SD 7003 (see Figure 4.12, t=0.639s). During the rest of the upstroke, the vortex shedding is very similar for ellipses (e=1%c and e=12%c) and SD 7003 profiles. In addition, the leading edge and trailing edge vortices detach completely from the airfoil (see Figure 4.12 at t=0.664s).

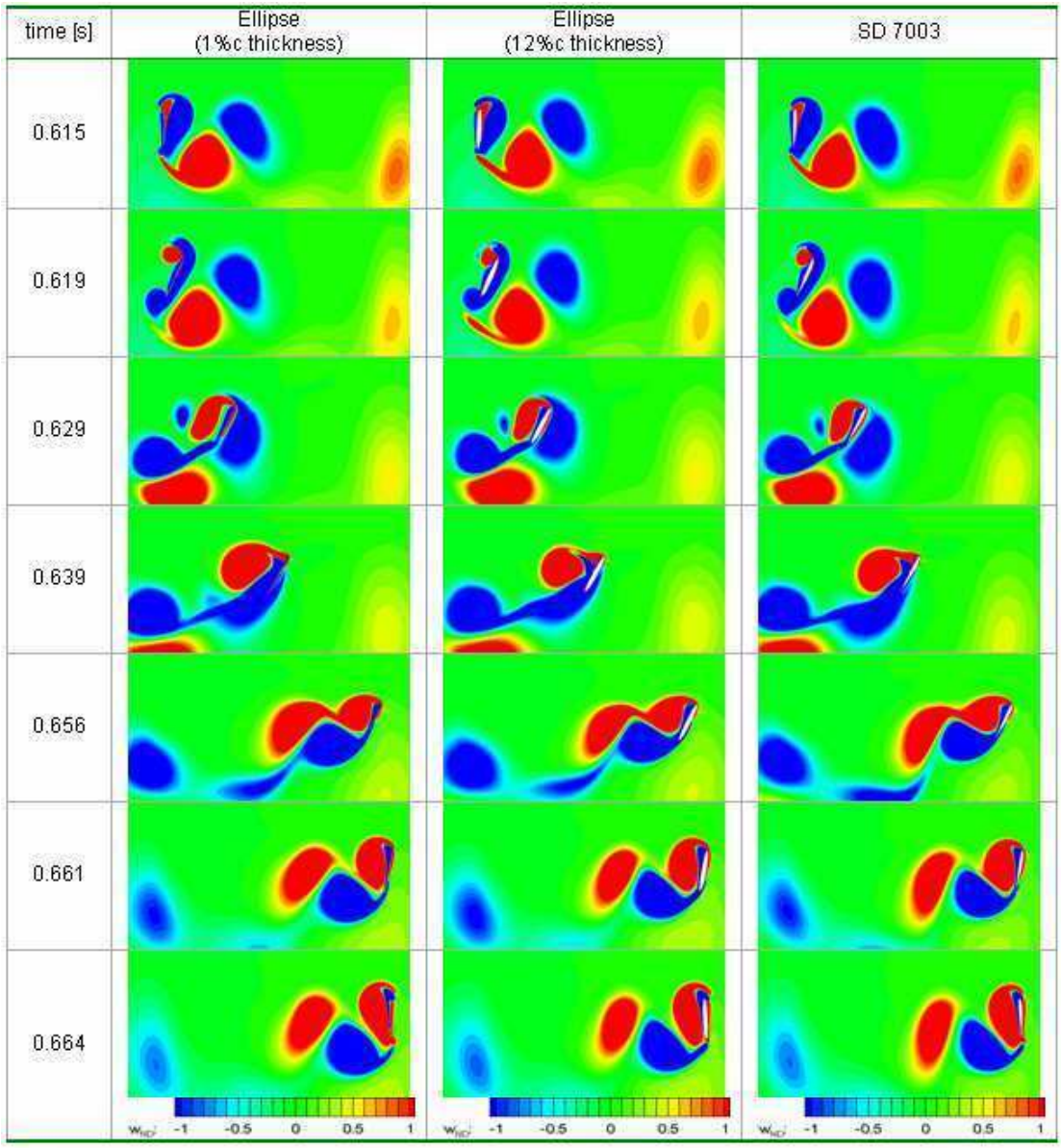

Figure 4.12 Instantaneous vorticity contours of profiles for a=c/2, $\alpha=60^{o}$, during the 7^{th} period of the flapping motion.

For ellipse (e=12%c) at a=c/2, a study is performed to see which initial angle of attack (α_0) gives the best mean lift coefficient ($\overline{C_L}$) value. $\overline{C_L}$ of the given α_0 is presented in Table 4.3. As it is noted in Table 4.3, there is an optimum α_0 value to get high $\overline{C_L}$ value. Up to $\alpha_0=45^o$, $\overline{C}_L$ increases. At $\alpha_0=45^o$, $\overline{C}_L$ reaches its maximum value ($\overline{C}_L$=1.046). Then, it drops abruptly at $\alpha_0=50^o$ and there is an increment between $\alpha_0=50^o$ and $\alpha_0=70^o$. Finally, it starts to decrease and reaches $\overline{C}_L$ = -0.098 at $\alpha_0=90^o$. Actually, due to the nature of hovering flight $\overline{C}_D$ should be zero during one period of the flapping motion, but there is certainly numerical errors and this error is getting larger for higher α_0 values.

Table 4.3 Mean aerodynamic coefficients of ellipse (e=12%c) for different α_0 at a=c/2.

α_0(deg)	$\overline{C}_L$	$\overline{C}_D$	**α_0(deg)**	$\overline{C}_L$	$\overline{C}_D$
5	0.101	-0.0011	50	0.817	-0.0021
10	0.229	-0.0013	55	0.826	0.0890
15	0.357	-0.0015	60	0.832	0.0079
20	0.489	-0.0019	65	0.875	0.1673
25	0.627	-0.0025	70	0.884	-0.2152
30	0.767	-0.0031	75	0.764	-0.2075
35	0.894	-0.0038	80	0.579	-0.3906
40	1.012	-0.0032	85	0.371	-0.0448
45	**1.046**	**-0.0031**	90	-0.098	-0.1150

The pressure distributions on the NACA 0012 and Ellipse (e=12%c) airfoils are shown in Figure 4.13. For these profiles, five different time instances are represented during the upstroke for $\alpha_0=30°$ and $\alpha_0=60°$ cases with the center of rotation at c/2. The pressure fields are also shown superposed with the instantaneous streamlines during the corresponding times in Figure 4.14.

It is observed that, at the beginning of the upstroke, the overpressure region in the domain due to the vortices from the previous stroke is more dominant for the ellipse case compared to NACA0012 (see Figure 4.14). At this time, the upper surface of the profile is fully dominated with the suction region. With the translation of the airfoil, there is a formation of strong suction region on the upper surface of the airfoil which further results in an increase in the lift coefficients during the translation phase. This increase in suction is also observable on the pressure coefficient distribution along the surface of the profile (Figure 4.13). In the meantime, the overpressure region on the lower surface of the airfoil also increases. At the mid-amplitude of the flapping motion, the airfoil's lower surface (leeward side) is entirely dominated by the overpressure region (red). However a small suction region is also observed at the lower surface of the ellipse close to the trailing edge.

At the inertial reference frame, the streamlines show that there is an important downwash induced on the airfoil when it is translating in the flowfield created by the two counter rotating vortices at the left and right hand sides of the domain. These vortices stay approximately in their positions for a half-stroke period until the airfoil returns back and pushes them downwards.

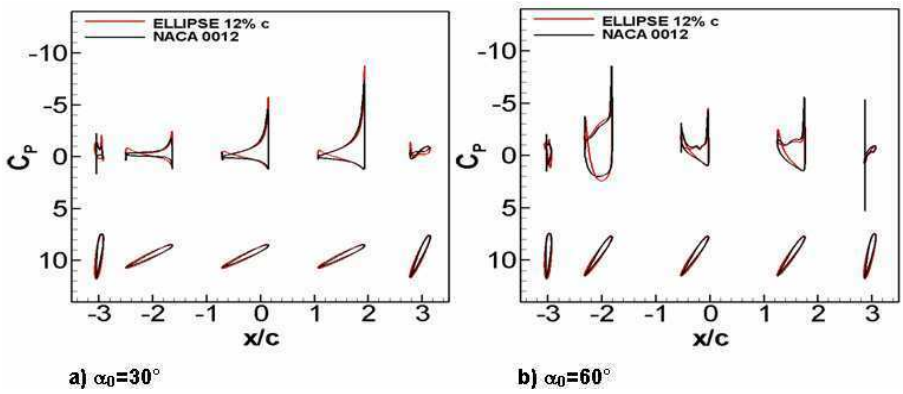

Figure 4.13 Pressure coefficient around the profiles (ellipse 12%c and NACA 0012) at different time instances during upstroke, a=c/2.

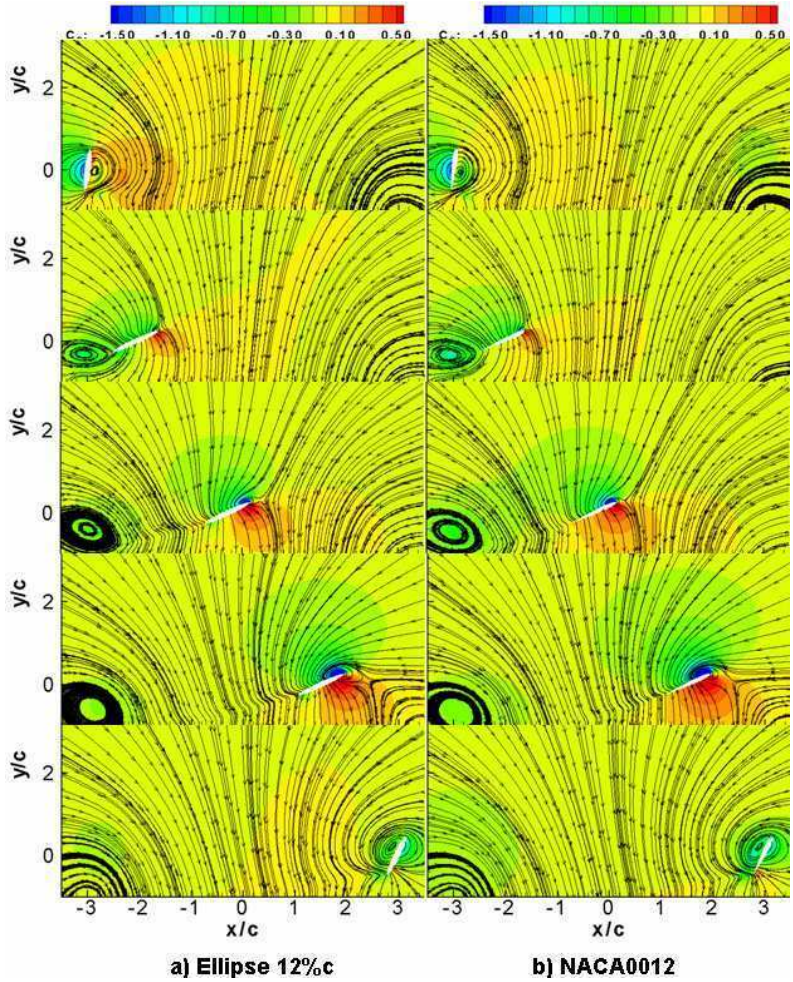

Figure 4.14 Instantaneous pressure coefficient (Cp) distributions for different profiles for α_0=30°, a=c/2.

4.1.2 Physics of Instantaneous Vortex Formation

In order to understand the physics of the problem, the variation in the vortex shedding mechanism close to the flapping airfoil is examined at this section. The distributions of pressure coefficients around the NACA 0012 airfoil are presented in Figure 4.15 for different angles of attack where the center of rotation is at c/2. The pressure coefficient distributions in the flowfield are also shown with the instantaneous streamlines in Figure 4.16. Same instances are represented in Figure 4.15 and Figure 4.16 during the upstroke. The centers of the vortices are also the locations for suction peak as can be observed from Figure 4.16.

At the beginning of the translational phase of the upstroke (2nd column in Figure 4.16), the overpressure region at the lower surface of the airfoil is very strong for α_0=60° and it covers the entire lower surface. This overpressure region is very weak for α_0=30° (see Figure 4.14) and it is only visible close to the leading edge at the beginning. The suction pressure on the upper surface of the airfoil is highly dominant by the two vortices generated at the leading and trailing edges of the profile. The upper surface suction pressure is also very strong for α_0=60° case.

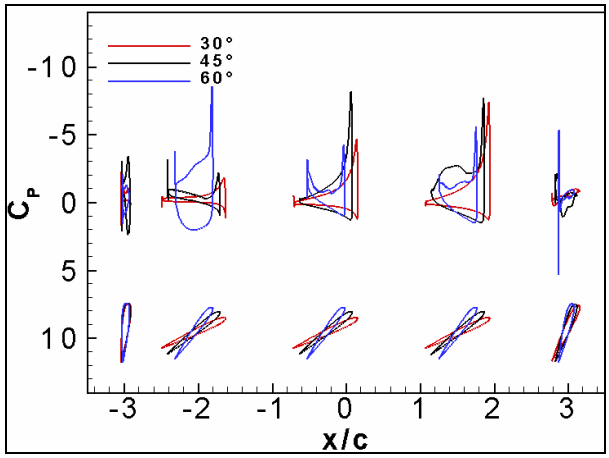

Figure 4.15 Pressure coefficient distributions around NACA 0012 at different time instances during upstroke at a=c/2.

At the mid location of the domain (3rd row in Figure 4.16), the upper surface of the airfoil is less dominated by the suction regions when compared to the beginning of the translational phase. Specially, for 30°, the suction has its highest value at the leading edge and diminishes towards the trailing edge on the upper surface. For 60°, there is still dominance of the trailing and leading edge vortices in addition to a detached leading edge vortex so the suction region on the upper surface is still observable.

At this time (t=0.637s), the overpressure region does not cover the entire lower surface of the airfoil for α_0=60°, which was the case for α_0=30°. At the end of the translational phase of the upstroke (4th row in Figure 4.16), the leading edge vortex

covers the entire upper surface of the airfoil resulting in a suction region throughout the upper surface for α_0=30°.

The suction region of the airfoil for α_0=60° case at this time (t=0.639s) is obtained by the combination of the leading and trailing edge vortices. Overpressure regions under the airfoil are similar for both cases.

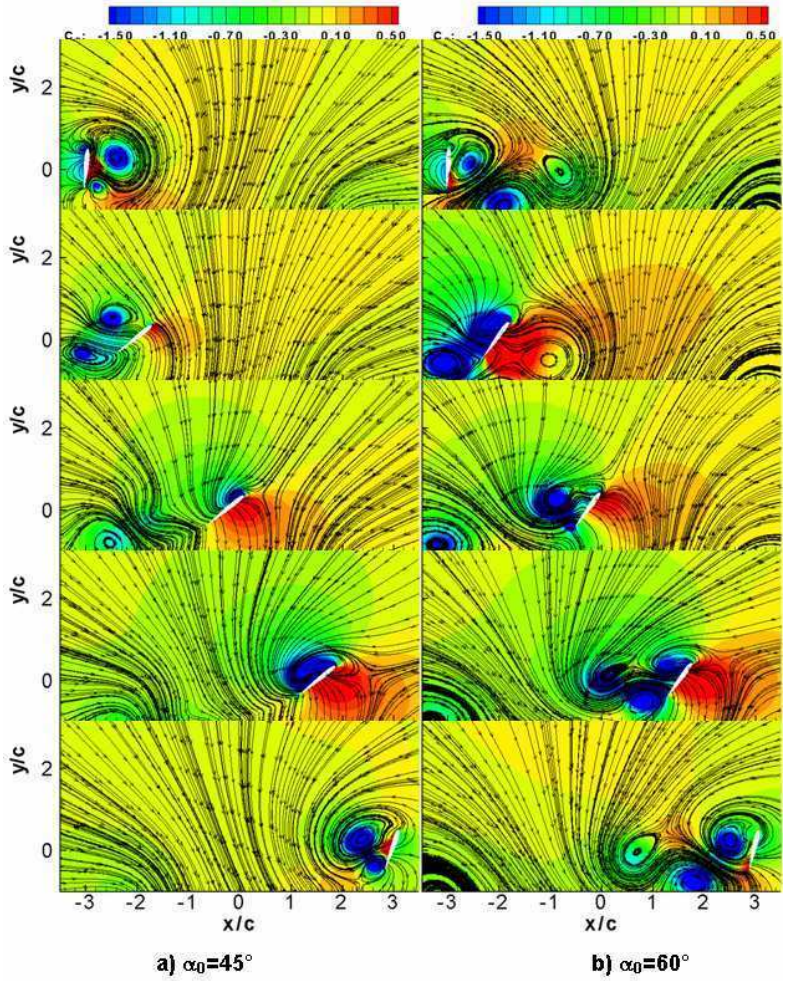

Figure 4.16 Instantaneous pressure coefficient (Cp) distributions of NACA 0012 for different α_0 at a=c/2.

The vorticity contours and relative streamlines for the time interval of local maximum lift coefficients are represented in the first and third columns (second row)

and for local minimum lift locations are represented in the second column (second row) of Figure 4.17. The streamlines are represented relative to the airfoils translational velocity. In this reference frame, the vortices on the upper surface of the airfoil are visible.

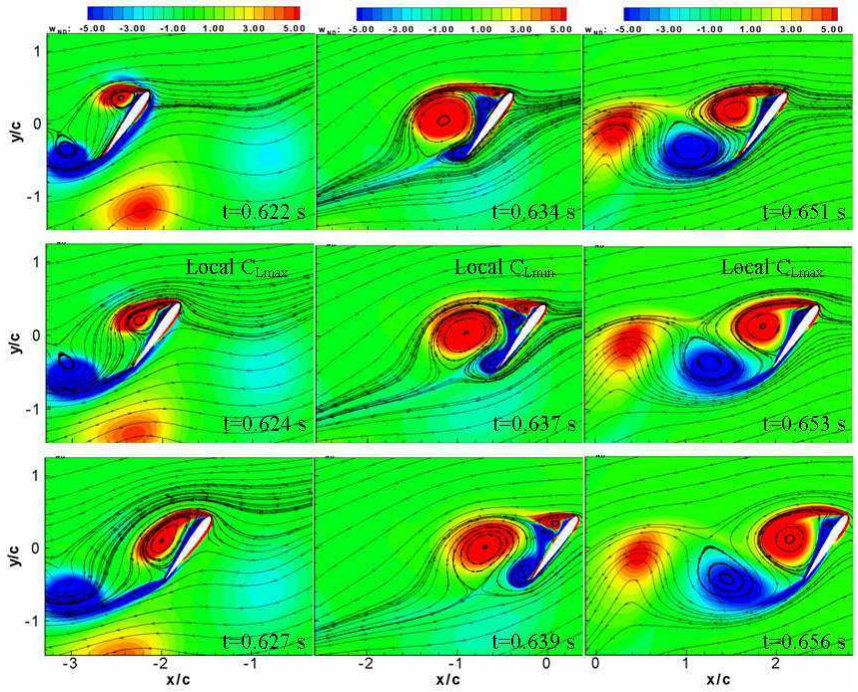

Figure 4.17 Vorticity contours represented with streamlines relative to airfoil's translational velocity for NACA 0012, a=c/2, α_0=60°.

Q contours represent the centre of the vortices shown with the relative streamlines (Figure 4.18). These vortices cause a suction region on the upper surface of the airfoil. The vortices on the upper surface of the airfoil at the leading edge cause a decrease in the suction region when they grow with the translation of the airfoil. This results in minimum lift coefficient at this time instant. At the maximum lift location the vortices form a strong suction region on the upper surface of the airfoil and the whole lower surface becomes an overpressure region.

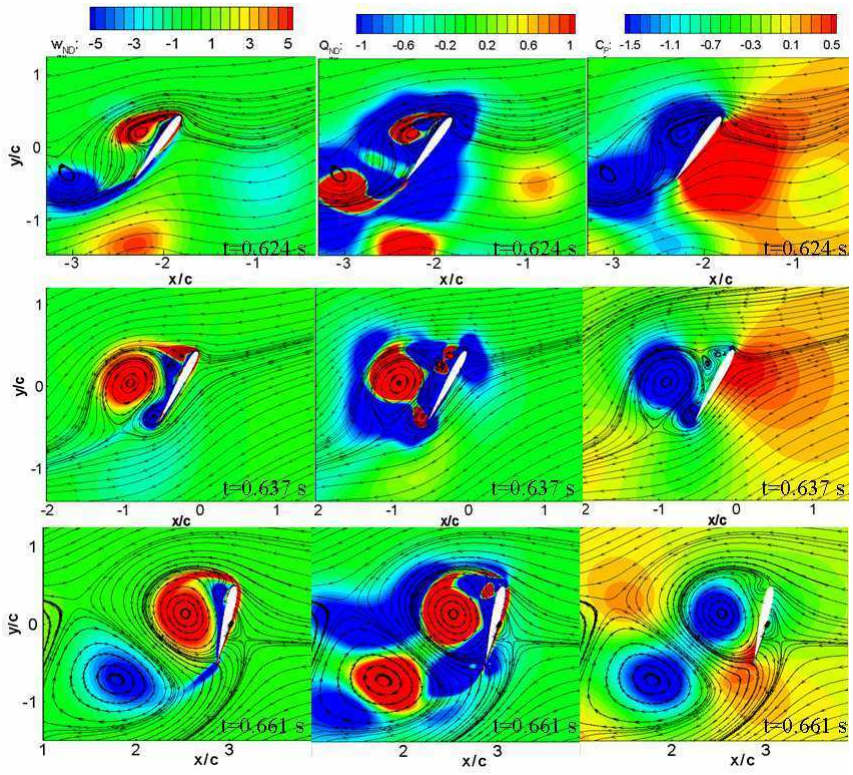

Figure 4.18 Vorticity, Q and C_P contours represented with streamlines relative to airfoil's translational velocity for NACA0012, a=c/2, α_0=60°.

Figure 4.19 shows the streamlines relative to the airfoil's translational velocity during the upstroke starting from the end of the rotational phase for α_0=60°. At t=0.622 s the profile is at the end of its pitching down motion until time t=0.625 s. After this time, it starts to translate with constant velocity and incidence up to t=0.652 s. At t= 0.654 s the profile restarts to rotate where it reaches 90^o angle of attack at the end of the upstroke. The shedding of leading edge vortices, the dynamic stall processes, is analyzed to understand the lift generation mechanism during the flapping motion. This shedding mechanism differs widely according to the α_0 parameter. The most interesting value of α_0 is found to be 60° since at this value the lift coefficient is very high at the beginning of the upstroke and decreases abruptly when compared to the smallest α_0 value at the end of the upstroke where the shedding of the leading edge vortices are very complex and abundant. Similar phenomenon is observed both in elliptic and NACA profiles for Re=1000.

In Figure 4.19, both streamlines relative to airfoil's translational velocity and C_L distribution of NACA 0012, at a=c/2, α_0=60° are presented. Some critical points during the upstroke are indicated in C_L distribution (see Figure 4.19). Following comments are for close-up sequences of Figure 4.19 (see Figure 4.20 (a-e)). At t=0.622 s, a clockwise leading edge vortex (LEV2) is forming on the upper surface of the airfoil where the airfoil is translating with $V(t)=0.91V_0$ and $\alpha(t)$=61°. At this time the lift and drag coefficients are calculated as C_L=2.02 and C_D= -3.18 respectively. At t=0.624s maximum lift occurs with the growth of LEV2. The first counter-clockwise leading edge vortex (LEV1) grows and occupies the first half of the upper surface of the airfoil at t=0.624 s and is still attached to all over the upper surface of the airfoil by surrounding LEV2 at t=0.627 s. With the growth of LEV2, the lift coefficient increases to a local maximum value of C_L=2.32 and the drag coefficient decreases slightly to C_D= -3.10 at t=0.624 s. As LEV2 grows, it causes the detachment of the LEV1 from the upper surface (leading edge) of the profile. Due to the effect of LEV2, LEV1 stretches and forms two counter clockwise vortices (figure of eight) which results once more in a single vortex with the translation of the airfoil at t=0.627 s. When the LEV1 covers the entire upper surface of the airfoil, the lift coefficient decreases to C_L=2.01 with a decrease as well in the drag coefficient (C_D= -2.57). At t=0.629s the trailing edge vortex (TV) forms. At t=0.631s LEV3 (ccw) forms, LEV1 detaches from the upper surface with the growth of LEV2 (cw) and TV. At t=0.634s LEV3 grows by pushing LEV2 towards TV. Another leading edge vortex (LEV4-cw) forms at t=0.637, and it completes the shedding of LEV1 from the airfoil. At t=0.639s LEV3 starts to detach from leading edge with the growth of LEV4. LEV2 and TV mix to form a unique vortex at t=0.642s. It is noted that as LEV3 (ccw) and LEV4 (cw) grow, C_L increases (see Figure 4.19, t=0.644s-t=0.649s). At t=0.649s LEV2 + TV vortex starts to detach from the trailing edge of the airfoil and at t=0.654s LEV2+TV vortex detaches completely from the airfoil due to growth of LEV3. This instant corresponds to the local C_{Lmax} value. At t=0.656s LEV3 covers the entire upper surface of the airfoil and C_L value starts to decrease.

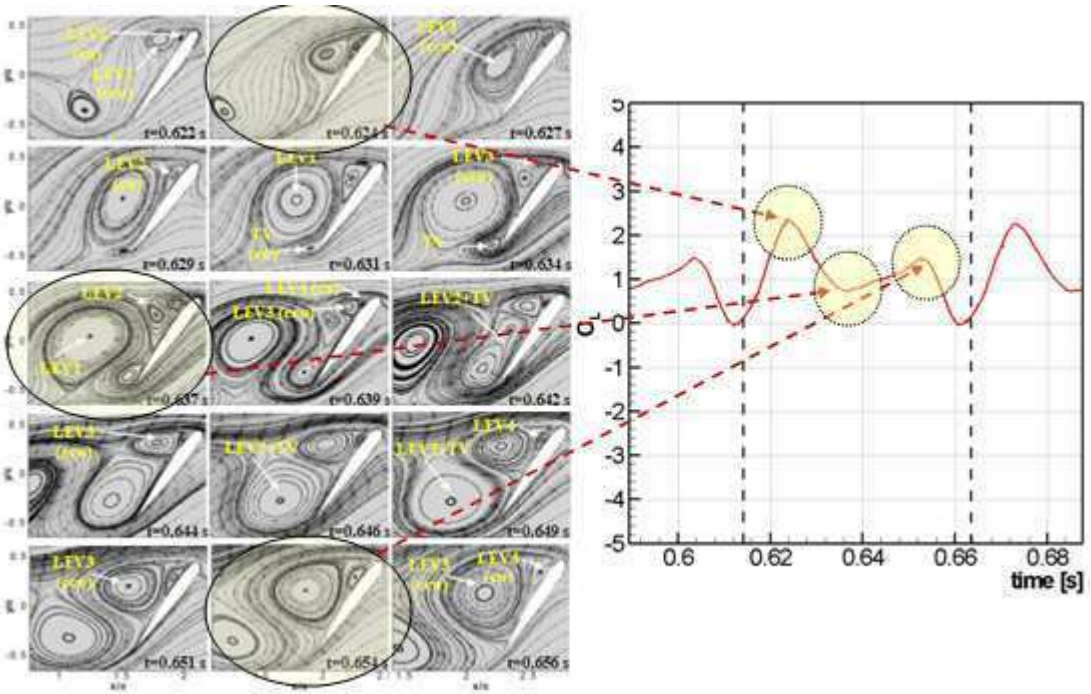

Figure 4.19 Streamlines relative to airfoil translational velocity and C_L distribution of NACA0012, a=c/2, α_0=60°.

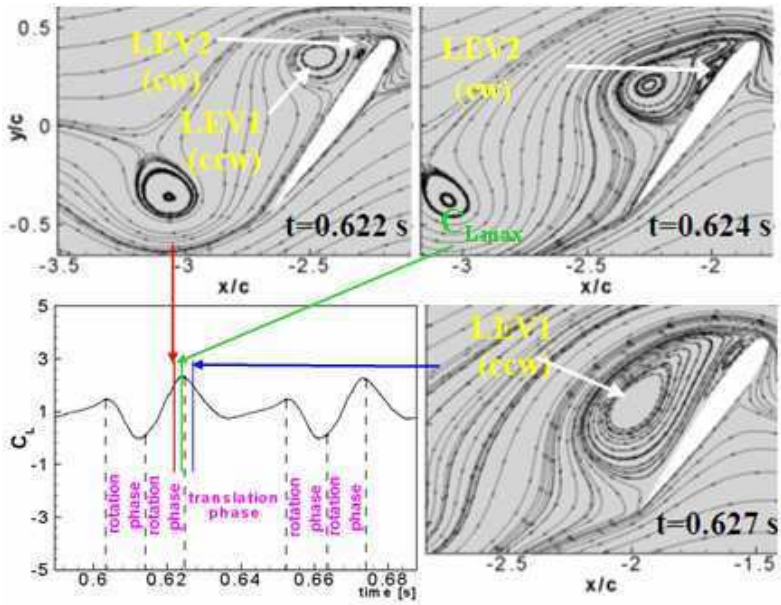

Figure 4.20 (a) Close-up Sequence of streamlines relative to airfoil translational velocity and C_L distribution of NACA0012, a=c/2, α_0=60° at indicated times (first row of Figure Figure 4.19).

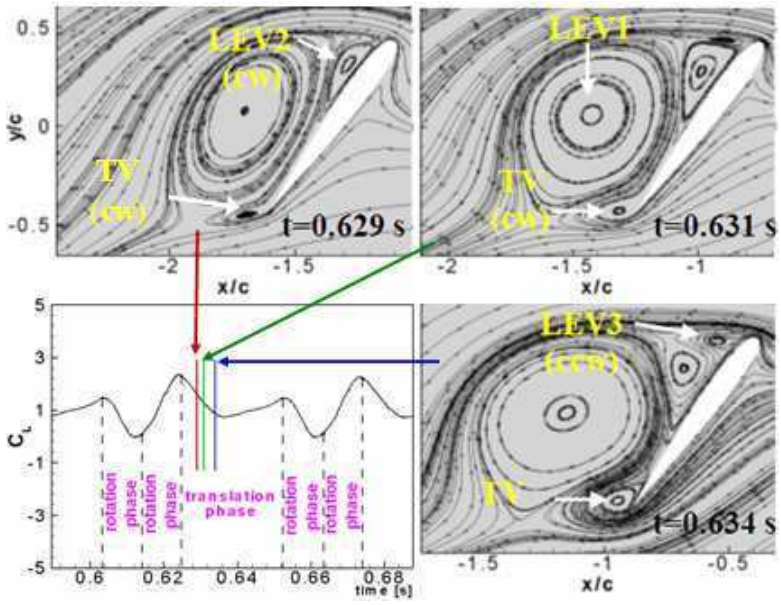

Figure 4.20 (b) Close-up Sequence of streamlines relative to airfoil translational velocity and C_L distribution of NACA0012, a=c/2, α_0=60° at indicated times (second row of Figure 4.19).

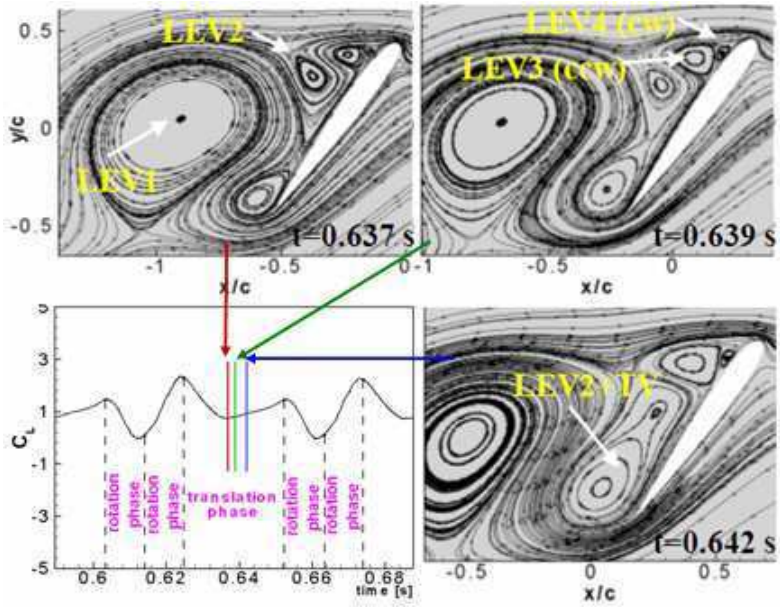

Figure 4.20 (c) Close-up Sequence of streamlines relative to airfoil translational velocity and C_L distribution of NACA0012, a=c/2, α_0=60° at indicated times (third row of Figure 4.19).

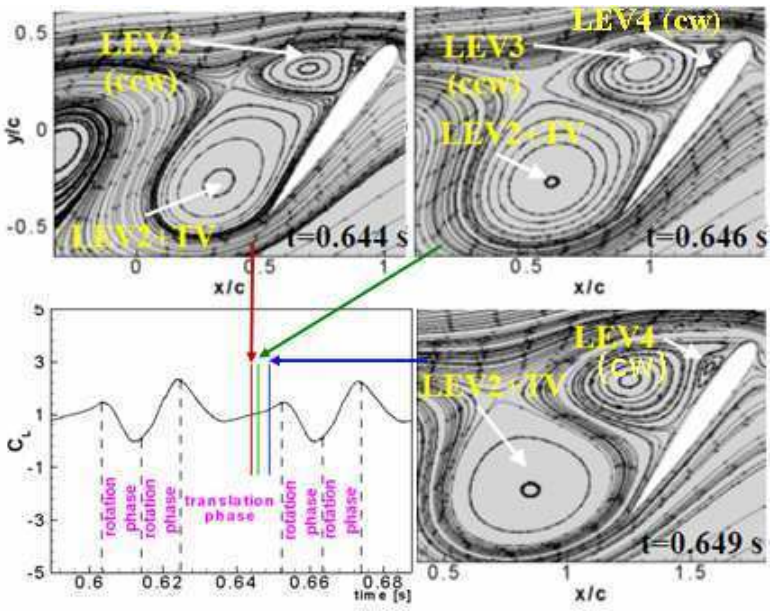

Figure 4.20 (d) Close-up Sequence of streamlines relative to airfoil translational velocity and C_L distribution of NACA0012, a=c/2, α_0=60° at indicated times (fourth row of Figure 4.19).

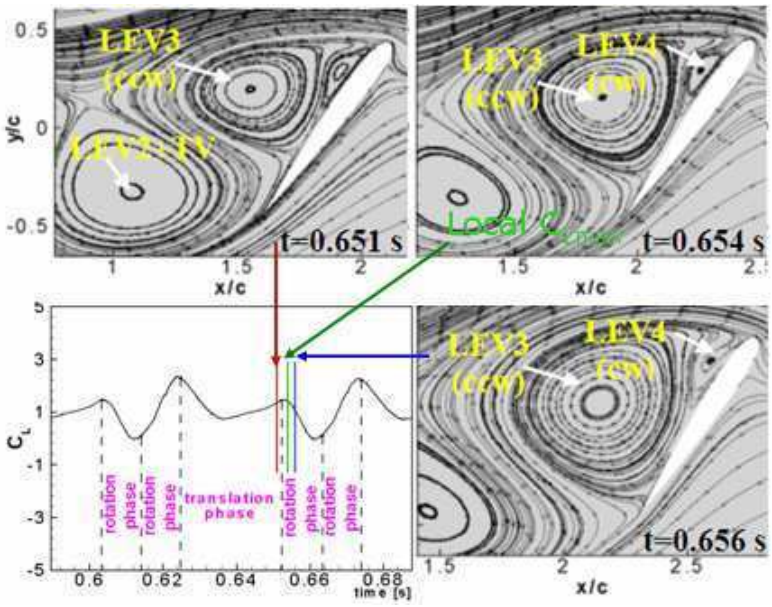

Figure 4.20 (e) Close-up Sequence of streamlines relative to airfoil translational velocity and C_L distribution of NACA0012, a=c/2, α_0=60° at indicated times (fifth row of Figure 4.19).

A similar presentation to Figure 4.19 is done for Ellipse (e=1%c) and SD 7003 profiles at prescribed instants (see Figure 4.21). The vortices on the upper surface (LEV1 and LEV2) and trailing edge (TV) of ellipse (e=1%c) is different than that of SD 7003 (t=0.629s-at the beginning of the translational phase of the upstroke).

At t=0.637s TV forming on ellipse (e=1%c) is stronger, and a new leading edge vortex (LEV3) forms at this time on the profiles. At this time due to the effect of the vortex (LEV2) at the mid-upper surface of the profiles, LEV1 detaches from the upper surface. At t=0.639s LEV2 and TV start to merge, but the vortices formed on the ellipse (e=1%c) mix earlier than that on SD 7003 (at t=0.642s). Also, the leading edge vortex formations and their growth rates are different for ellipse (e=1%c) and SD 7003 (t=0.639s). At t=0.656s LEV2+TV covers the entire upper surface of the profiles and a distinct leading edge vortex forms on the upper surface of the ellipse (e=1%c).

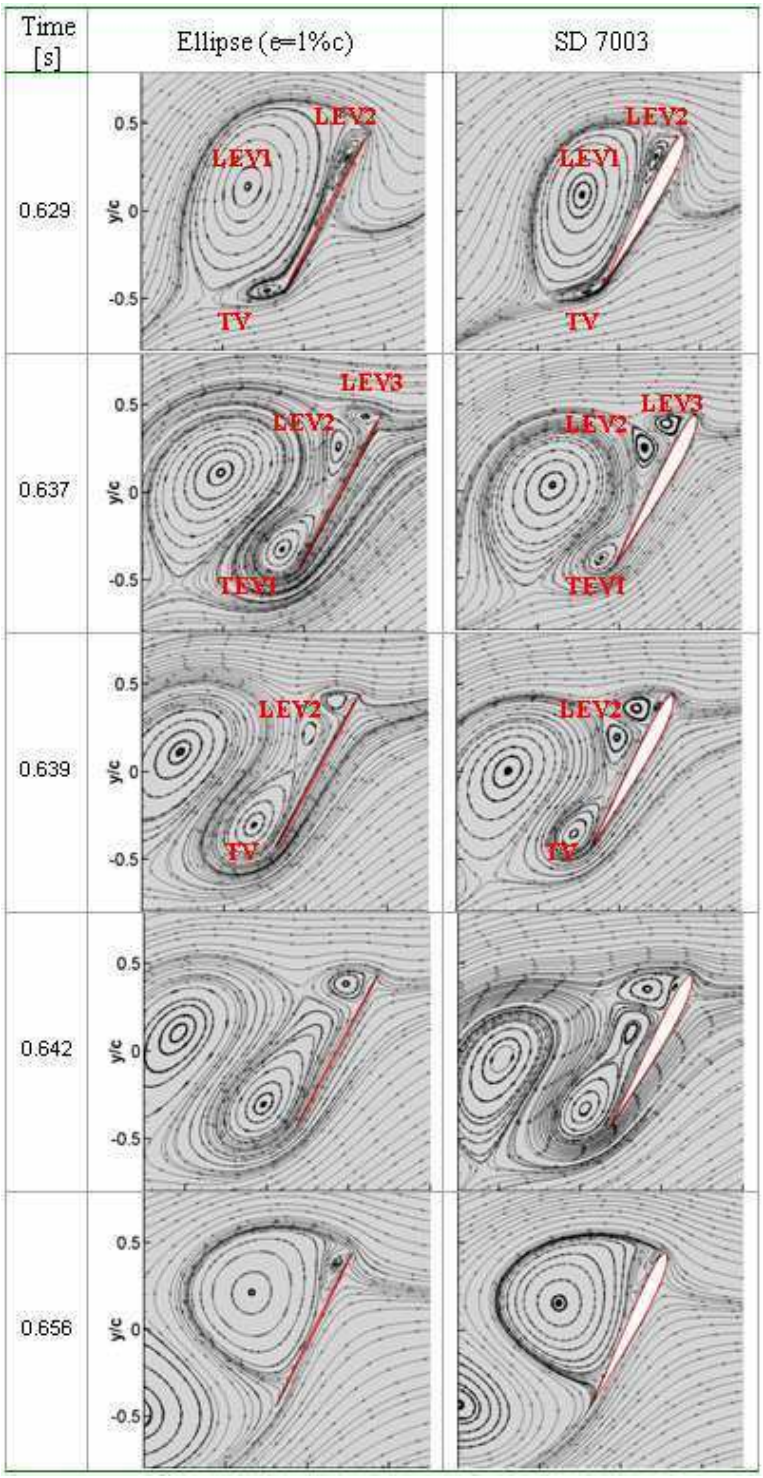

Figure 4.21 Streamlines relative to airfoil translational velocity for Ellipse (e=1%c) and SD 7003 profiles, a=c/2, α_0=60°.

4.2 Analysis of Type B Flapping Motion [46]

In this part of the study, "Type B" flapping motion defined in Chapter II is implemented to an elliptic profile (e=12%c) having 0.01m chord length. The works of Wang et al. [3] cover a 2D numerical calculation and comparison with 3D experimental results in view of aerodynamic force coefficients.

For the simulation of flapping kinematics of Wang et al. [3], an ellipse of 12% chord thickness is used (c=0.01m). The effects of profile shape and thickness of the profiles on the aerodynamic forces and vortex shedding mechanism of the prescribed flapping motion was analyzed in the previous study [2]. It is found that the use of elliptic profiles and NACA airfoil profiles with 9%c and 12%c thicknesses do not differ much from the aerodynamic force coefficients view point at a Re number of 1000.

Same numerical solution technique and computational grid domain as used in the previous study [2] is employed for all computations of the present study.

An analysis on sinusoidal flapping motion [46] is performed with the described kinematics in order to investigate the effect of these parameters on the aerodynamic force coefficients. In order to obtain the defined *Re* values; frequency, *f*, is calculated as $f = \mathrm{Re}\,\nu / \pi c A_0$.

Table 4.4 Investigated Parameters

	A_0/c	*Re*	*f [Hz]*
Case 1	2.8	75	1.240
Case 2	2.8	115	1.900
Case 3	2.8	200	3.306
Case 4	4.8	115	1.109

4.2.1 Evaluation of Unsteady Flowfield and Aerodynamic Forces

Sinusoidal angle of attack and velocity distributions of the motion for Case 2 and Case 4 are presented in Figure 4.22 to show the difference of the kinematics by the change of A_0/c value. The frequency of the former is approximately twice of the later one.

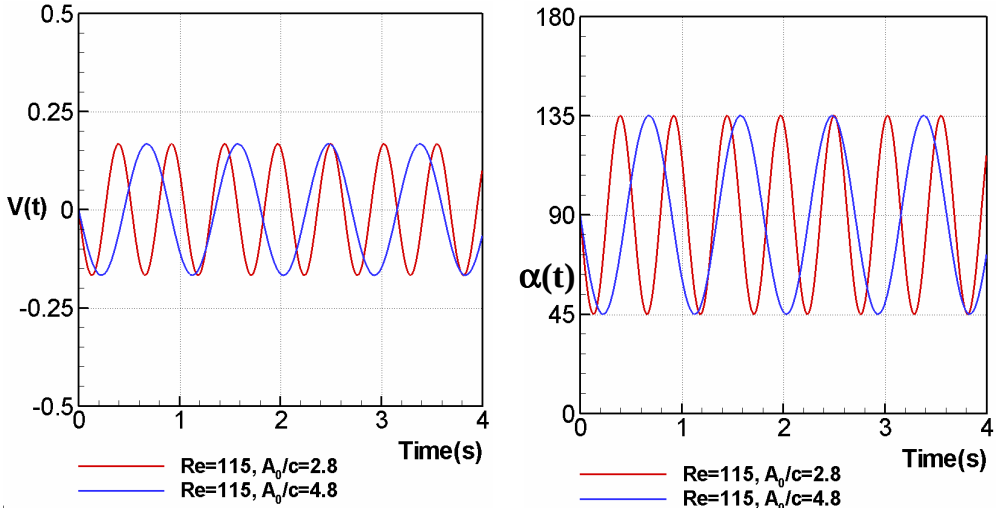

Figure 4.22 Instantaneous velocity and angle of attack (α(t)) distribution vs. time for case 2 and case 4.

In the figures below, time is non-dimensionalized with respect to the flapping period of the case.

In Figure 4.23, the computed forces obtained from the present study are compared with the experimental and empirical data of Wang et al. [3]. The empirical data is carried out by using the Eqs. 3.18-3.19 based on the translational velocity. The forces are normalized by the maxima of the corresponding quasi-steady forces [3]. For lift coefficient distribution, although there is a slight over estimation at the mid-strokes, the present computations catch the C_L values of the experiment during translation of the wing (see Figure 4.23). Also, the present computations estimate the right rotation position as in the experiment. For drag coefficient, it is observed that the general

behavior of the distribution obtained by the present computations is very similar with that of the experiment [3]. Especially in the translational phase, they are very successful. Generally, it is noted that the present computations are very good at estimating the force coefficients of this problem.

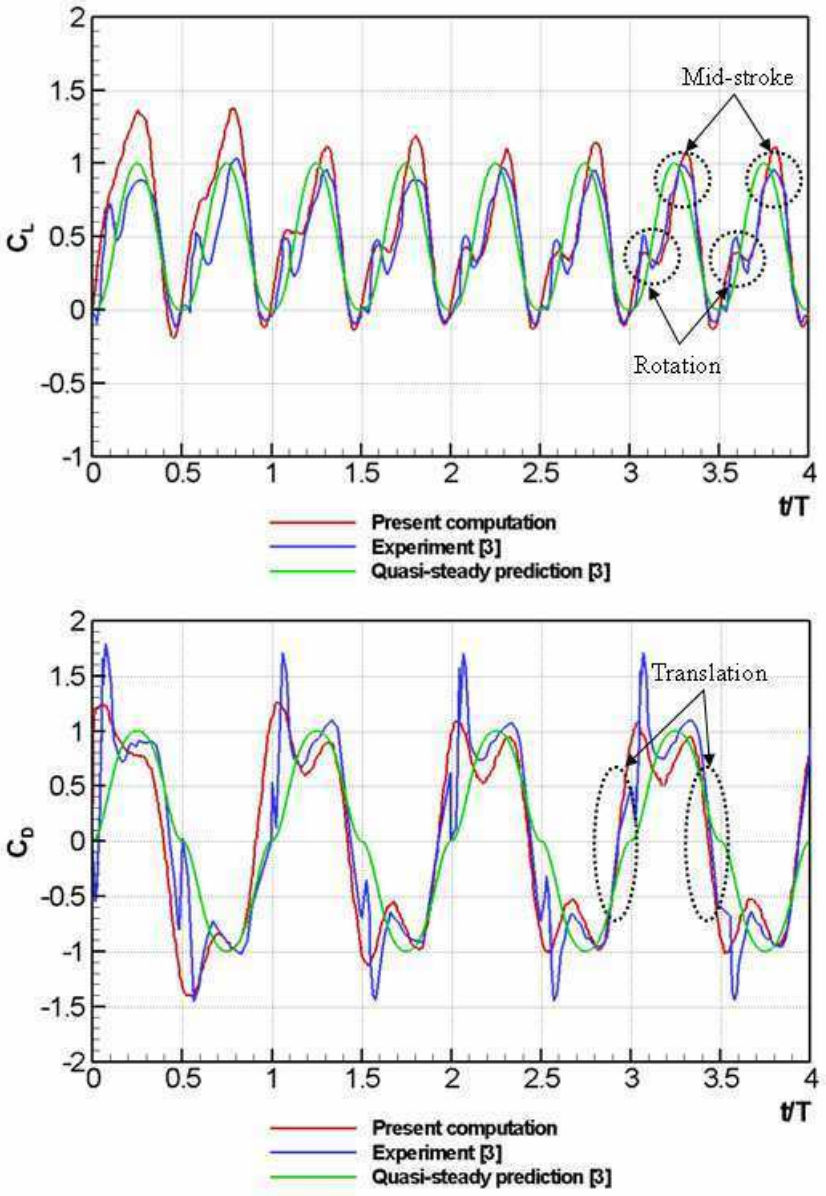

Figure 4.23 Lift and Drag coefficients comparison between experiment [3], present computation and quasi-steady estimations [3] for symmetric (φ=0) rotation, Re=75, and A_0/c=2.8. Time is non-dimensionalized with the flapping period of the case 1.

The lift and drag coefficient distributions of the two cases are represented in Figure 4.24. The effect of stroke amplitude on the aerodynamic force coefficients is observed by keeping the Reynolds number constant to Re=115. While C_L distributions converge to each other in time, same behavior is not observed for C_D distributions. By keeping the stroke amplitude constant ($A_0/c=2.8$), the effect of Reynolds number on the aerodynamic force coefficients (C_L and C_D) is analyzed in Figure 4.25. It is noticed that the effect of stroke amplitude is more significant than the effect of Reynolds number on drag coefficients. This effect is also observed in vorticity distribution (Figure 4.26).

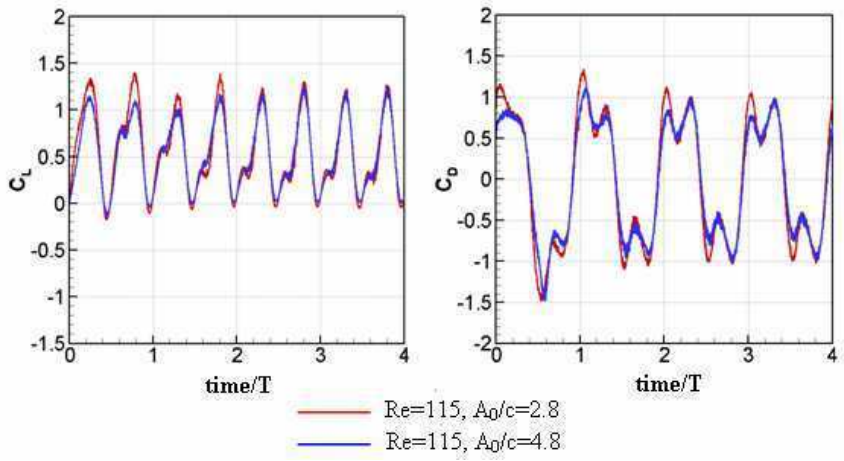

Figure 4.24 Computational lift and drag coefficients Re=115, $A_0/c=2.8$ and 4.8.

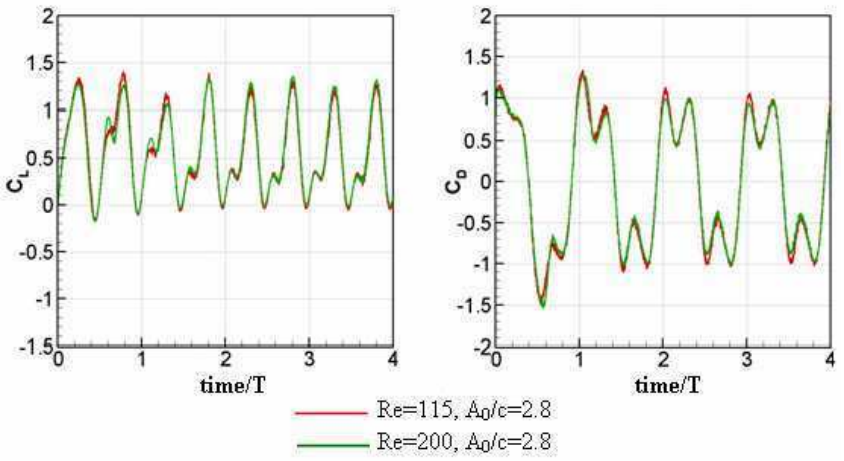

Figure 4.25 Computational lift and drag coefficients for $A_0/c=2.8$, Re=115 and 200.

It is found that as the amplitude increases, trailing edge vortex trace at the end of the stroke (blue region at t/T=4 and red region at t/T=4.5) detaches from the airfoil surface quicker (Figure 4.26). Drag coefficient is at its maximum at this time instant and lift coefficient is approximately zero. The leading edge vortex grows quicker for higher amplitudes as can be seen at t/T=4.1 time instant during downstroke and at t/T=4.6 during upstroke. The quick growth of the leading edge vortex towards the trailing edge pushes more translational vortex far from the airfoil surface (red contours at t/T=4.3 and blue contours at t/T=4.8). At the end of the stroke airfoil enters to the trace of trailing edge vortex generated at the beginning of the stroke. And this trace is more dominant for $A_0/c=2.8$ then $A_0/c=4.8$ (last row in Figure 4.26).

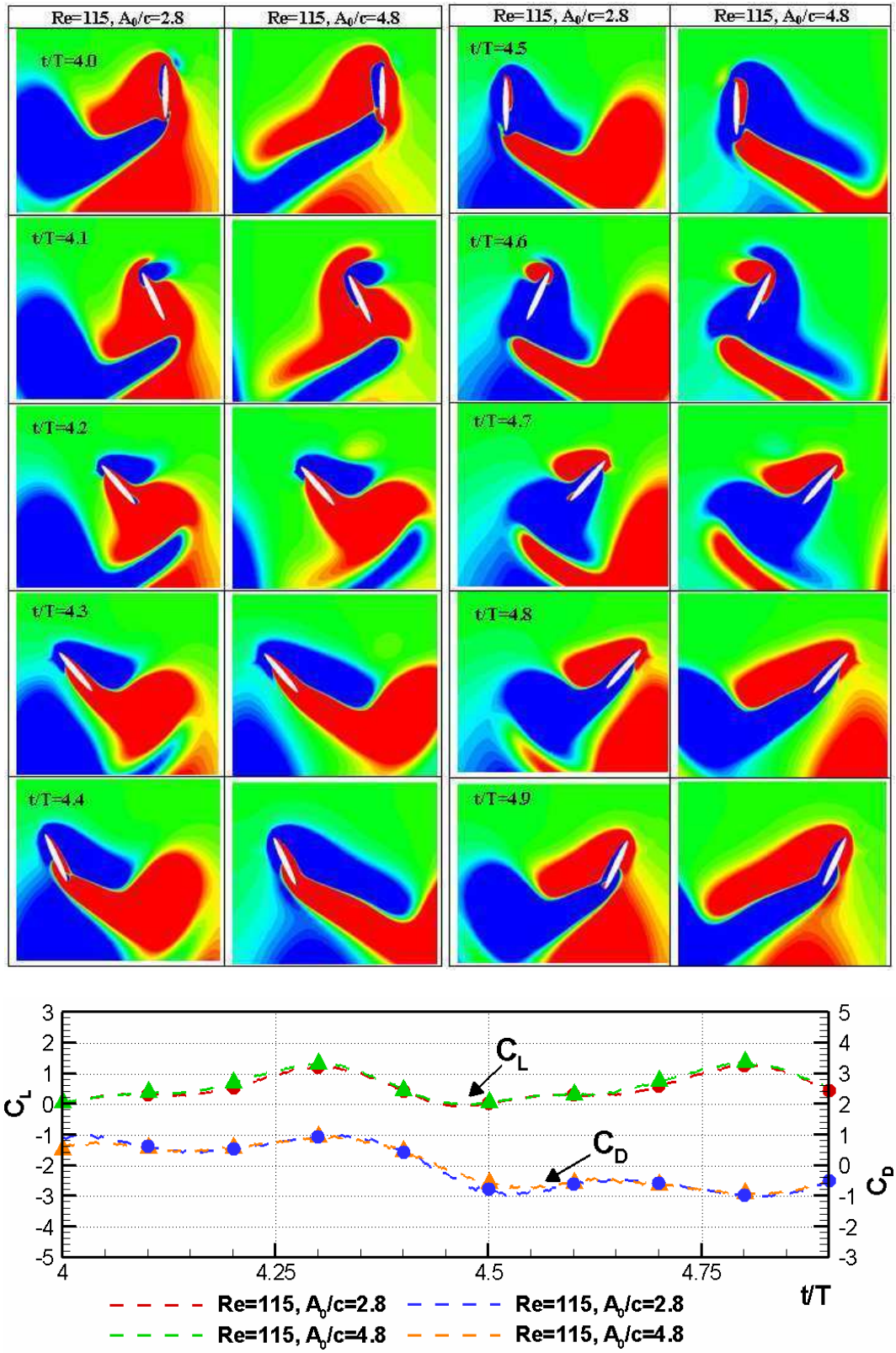

Figure 4.26 Instantaneous vorticity contours and aerodynamic force coefficients for case of A_0/c= 4.8 and A_0/c= 2.8 at Re=115, φ=0 during 5th period.

A comparison between computation and experiments of Wang et al. [3] and the present computational results is will be presented for the case of $A_0/c=4.8$ and Re=115. In the first column of Figure 4.27 2D computational results [3]; in the second column 3D experimental results in a 2D slice at 0.65R taken from DPIV measurements [3] and in the third column 2D computational results of the present study are represented respectively in columns 1 to 3 of Figure 4.27. Ten different time sequences are shown during the fourth stroke for each case. Time is non-dimensionalized with the flapping period of the case.

The vorticity contours are presented (see Figure 4.27) to show the major features of vortex dynamics through a complete stroke cycle. When the three results at each indicated time steps are compared, it is seen that the major features of vortex dynamics are similar. The color scale for vorticity of computation and experiments [3] did not correspond to the exact same contour values. Due to lack of the color scale of vorticity contours achieved by Wang et al. [3], the figure of our computational results and their results should be viewed more qualitatively than quantitatively.

Notice that even though the kinematics of left and right strokes is identical, the flow fields for each case differ slightly for the computational results of Wang et al. [3]. However, this discrepancy in the flow field is not observed in our computational results.

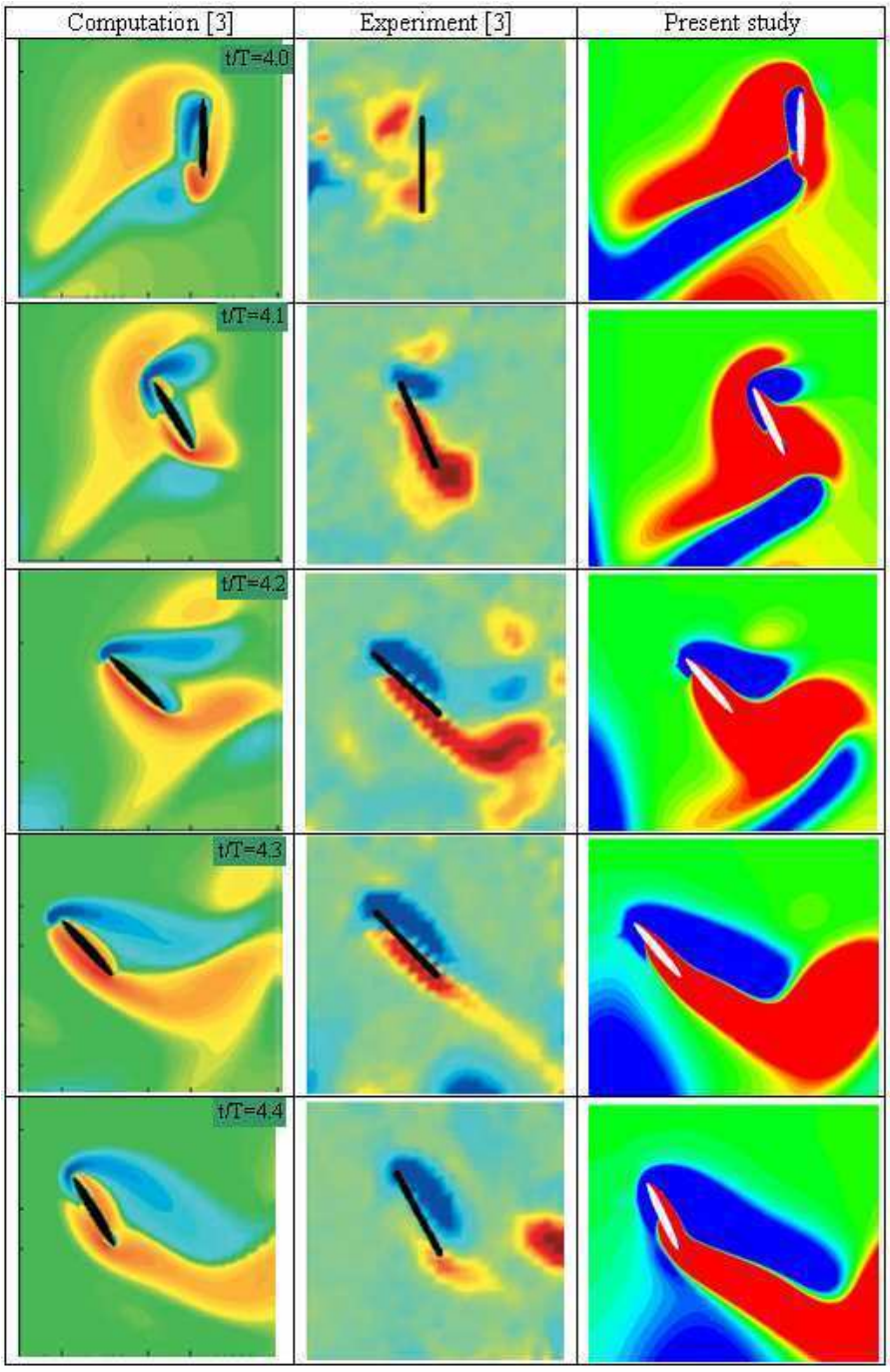

Figure 4.27 Instantaneous vorticity contour for case of A_0/c= 4.8, Re=115, φ=0. First two columns are the results of Wang et al. [3] and the third column is the results of the present study.

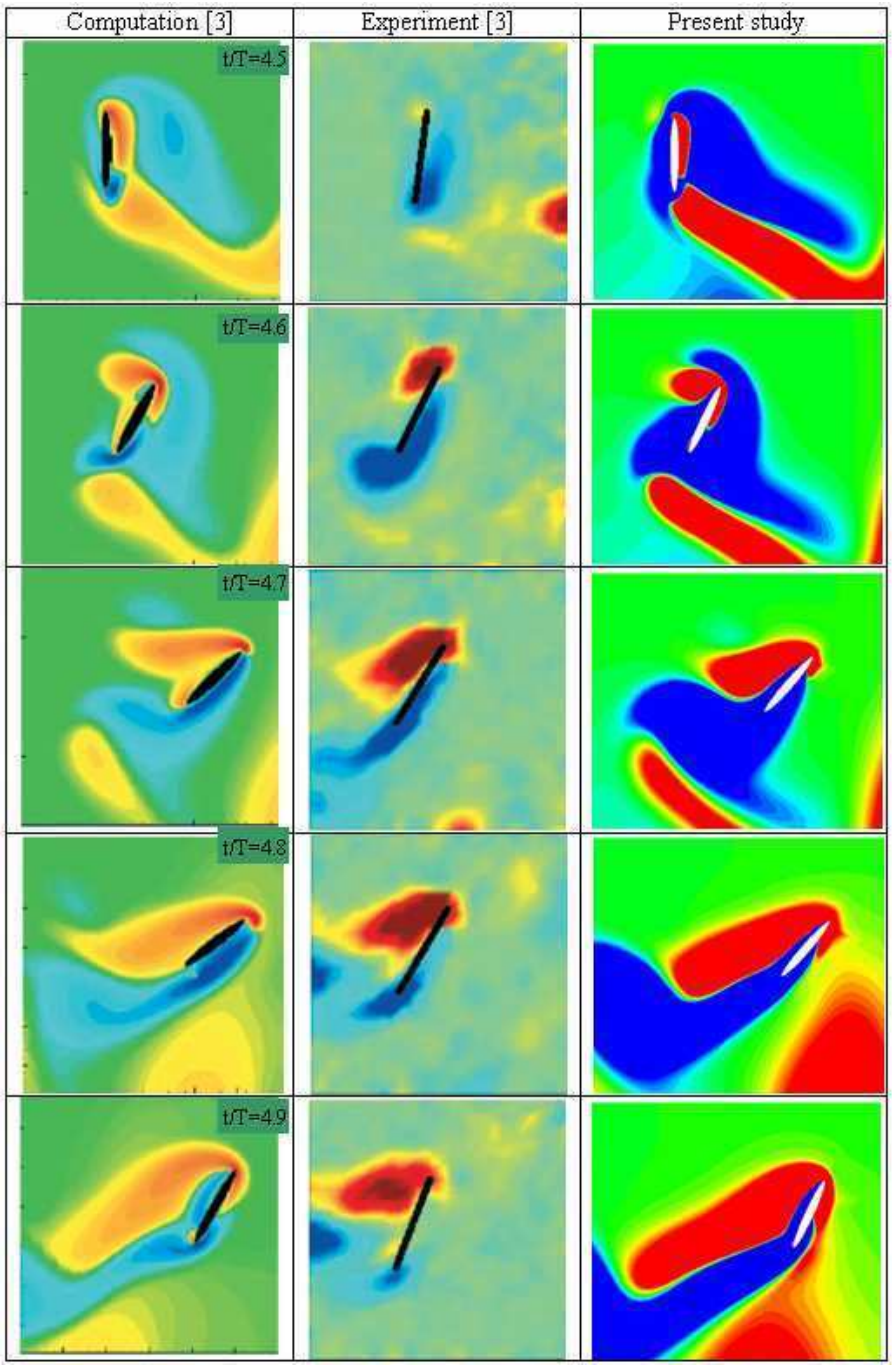

Figure 4.27 (Cont'd) Instantaneous vorticity contour for case of A_0/c= 4.8, Re=115, φ=0. First two columns are the results of Wang et al. [3] and the third column is the results of the present study.

Also a comparative study is performed between the flapping motions prescribed by Kurtulus et al. [1] (Case A) and Wang et al. [3] (Case B) for the same Re number of 1000 by keeping the mid-stroke amplitude angle of attack α_0 and A_0/c constant.

Flapping motions are applied to an ellipse wing section having c=0.01m chord length and e=12%c thickness. Present grid domain is used for both computations. Some parameters used in computations and calculated $\overline{C_L}$ and $\overline{C_D}$ values are presented in Table 4.5. Mean lift and drag coefficients ($\overline{C_L}$ and $\overline{C_D}$) are calculated for 7th period of both motions according to Eqs. 3.12-3.13. For same Re number, amplitude (A_0/c) and same 45° angle at the mid-stroke, it is found that the mean lift coefficient of Case A is twice that of Case B.

Table 4.5 Investigated Parameters

	Case A Kurtulus et al. [1]	**Case B Wang et al. [3]**
Re	1000	1000
Period, T [sec]	0.098	0.130
A_0/c	6	6
α_0 [^{o}]	45^o	45^o
$\overline{C_L}$	1.046	0.501
$\overline{C_D}$	-0.0031	0.0083

4.3 Analysis of Type C Flapping Motion

In this part of the present study, “Type C” flapping motion defined in Chapter II is implemented to an elliptical wing section having 1.6mm thickness and 0.0254m chord length. Freymuth [4] performed a three-dimensional experimental study to analyze the dynamic stall vortices and the thrust coefficient which may also be considered as a lift coefficient of the hovering airfoil motion since thrusting during actual hovering would be upward. A planar airfoil having a thickness 1.6mm with rounded edges, chord length 2.54 cm and span l=30cm is used in the experiments. Density is less than $1kg/m^3$ at Boulder where experiments were performed.

4.3.1 Evaluation of Unsteady Flowfield and Aerodynamic Forces

Sinusoidal variations angle of attack and velocity distributions of the motion for mode 1 are presented in Figure 4.28. Mode 1 and Mode 2 flapping motion prescribed by Freymuth [4] (Figure 3.8-Figure 3.9) are applied to the wing model. In Figure 4.29 and Figure 4.30, force coefficient computed by using the present numerical method is compared with the experimental data of Freymuth [4]. The computed lift is non-dimensionalized according to Eqs. 3.21 and 3.22. Due to some differences (e.g. wing model, density etc.) between the present study and Freymuth’s experiment [4], most efficacious consistency is not provided. This is because of three dimensional effect of the experiments [4]. Especially, due to high frequency there is more numeric error. The present computation is generally good at estimating the C_L value of the experiment (see Figure 4.29 and Figure 4.30).

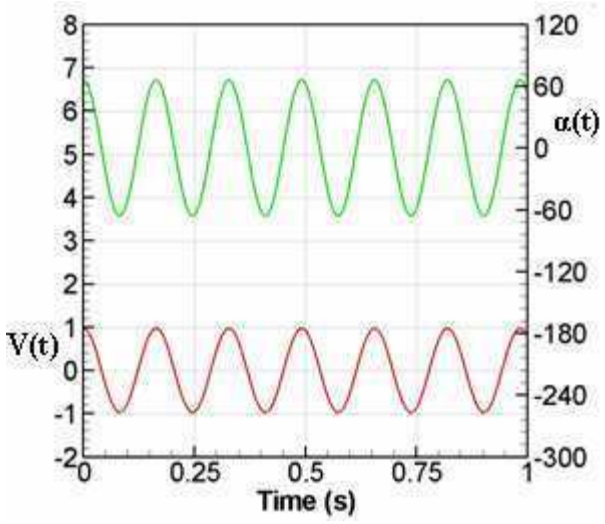

Figure 4.28 Instantaneous angle of attack (α(t)) and velocity distribution vs. time for mode 1 hovering.

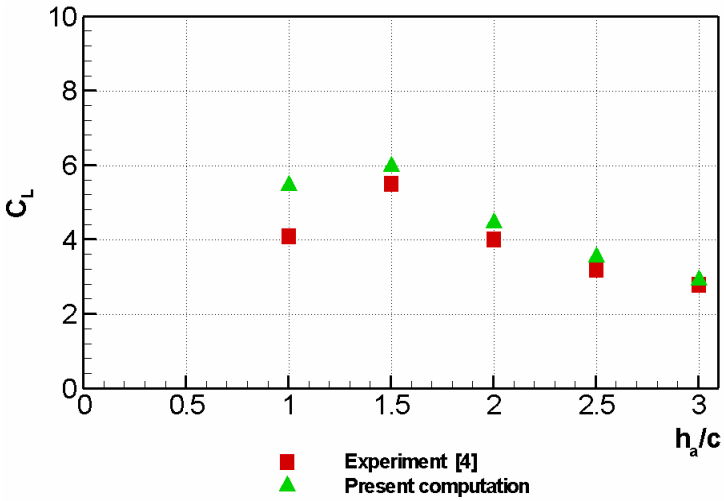

Figure 4.29 Lift coefficient comparison between experiment [4] and present computation for mode 1, $\alpha_a=66^o$, $\alpha_0=0$, $\varphi=90$ and $R_f=1700$.

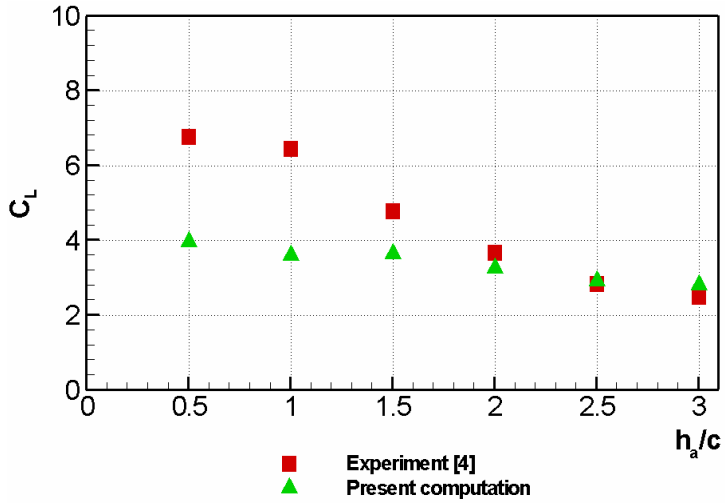

Figure 4.30 Lift coefficient comparison between experiment [4] and present computation for mode 2, $\alpha_a=25^o$, $\alpha_0=90$, $\varphi=-90$ and $R_f=1700$.

Entire cycle of airfoil flapping in Mode 1 with $\alpha_a=66^o$, $h_a/c=1.5$ is shown in Figure 4.31 (a-b). Black and white pictures belong to Freymuth's experiment [4]. Flow visualization was by means of the titanium-tetra-chloride method described by Freymuth et al. [47]. Colorful pictures are results of the present study. Frames are ordered into columns from top to bottom and columns are ordered from left to right. Time between consecutive frames is $\Delta t=1/16s$. One should analyze the pictures by following the first and second columns together. First row of left two columns show the farthest right position of the airfoil (lower right corner of the frames). From this position to the bottom of the third and fourth columns, the airfoil moves its left position. During this movement, airfoil creates a clockwise (blue) rotating vortex which is very similar with the experiment [4] (see Figure 4.31 (a)-indicated in the last row). In columns 1 and 2 of Figure 4.31 (b), the airfoil moves to the right. The previously generated clockwise (blue) rotating vortex (see Figure 4.31 (a)-indicated in the last row) starts to detach from the upper surface of the airfoil and moves upward. And a new counterclockwise (red) rotating vortex is formed and grows (see Figure 4.31 (b)-indicated in the last row). This process repeats during each cycle and results in an upward moving vortex street. These vortex formations were observed in the experiment also [4].

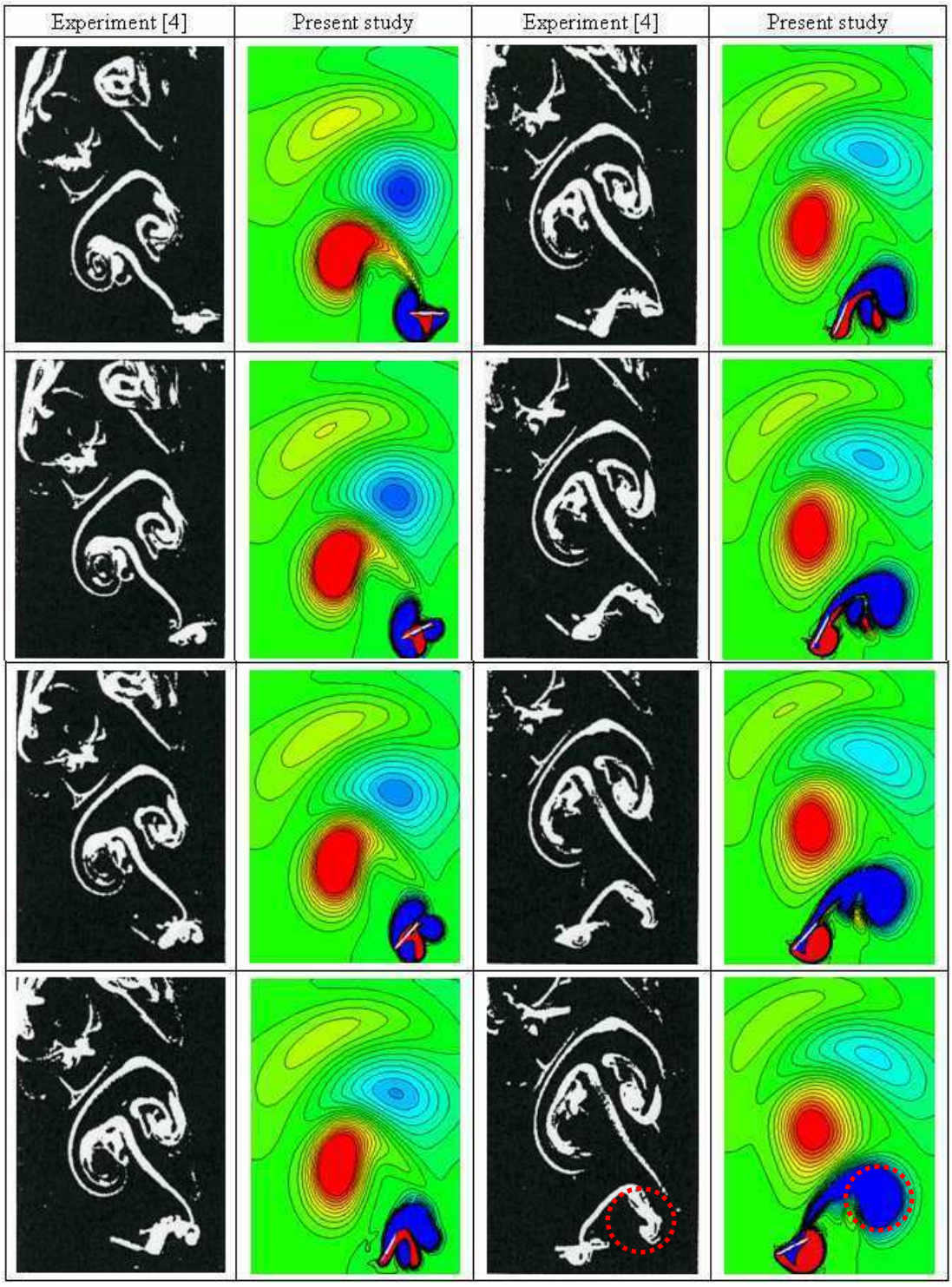

Figure 4.31(a) Instantaneous vorticity contours for Mode 1. Black and white pictures are results of Freymuth [4] and the colorful pictures are results of the present study. $\alpha_a=66^o$, $h_a/c=1.5$, $R_f=340$, f=1Hz., $\Delta t=1/16$s.

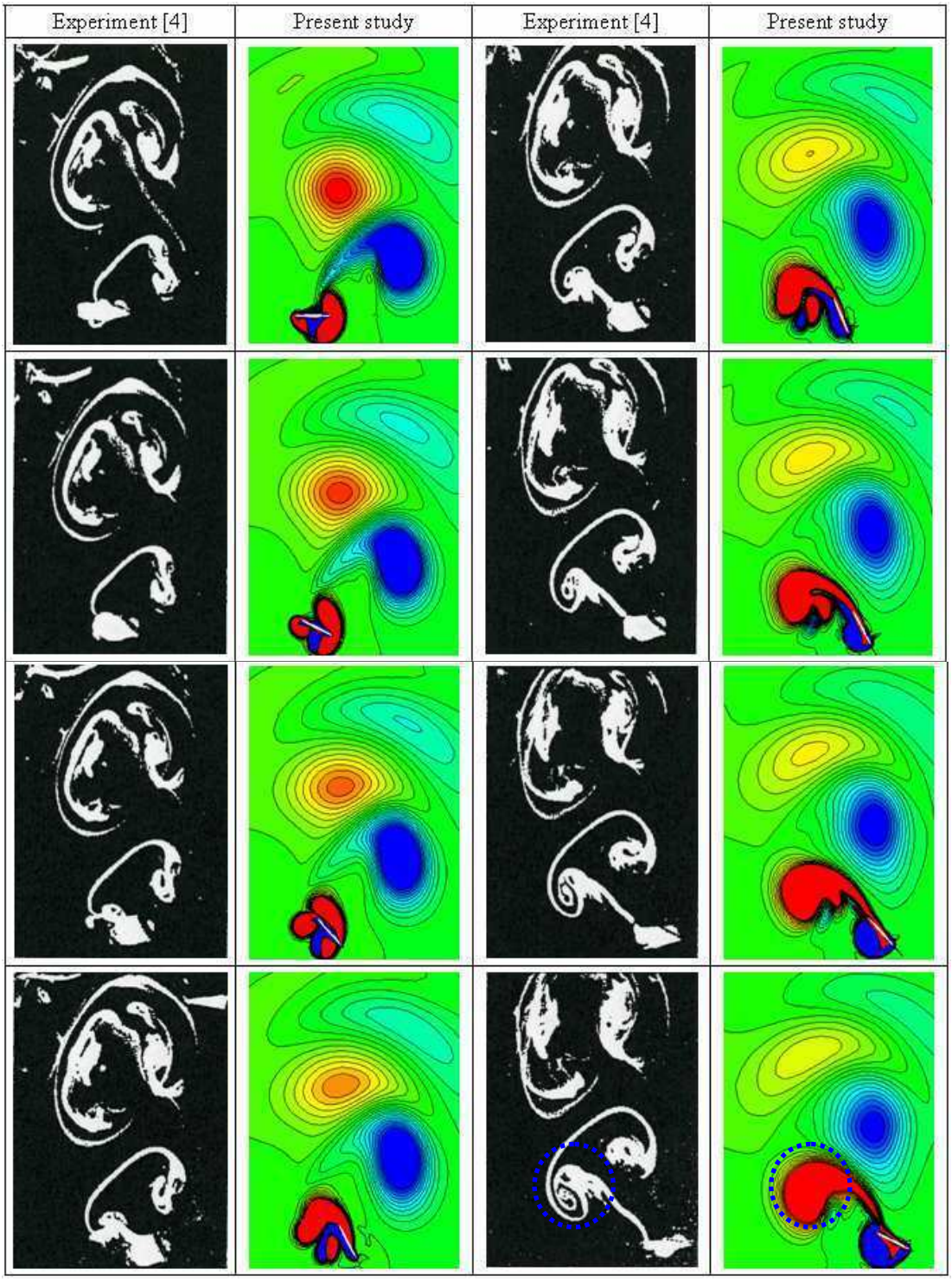

Figure 4.31 (b) Instantaneous vorticity contours for Mode 1. Black and white pictures are results of Freymuth [4] and the colorful pictures are results of the present study. $\alpha_a=66^o$, $h_a/c=1.5$, $R_f=340$, f=1Hz., $\Delta t=1/16$s.

CHAPTER V

CONCLUSION

In this study, a detailed numerical investigation is performed to investigate the effect of some geometrical parameters, such as the airfoil profile shapes, thickness and camber distributions and as well as the flapping motion kinematics on the aerodynamic force coefficients and vortex formation mechanisms at low Reynolds number.

The numerical analysis tool is a DNS code using the moving grid option. Laminar Navier-Stokes computations are done for flapping motion using the prescribed kinematics in the Reynolds number regime of 1000. The flow field for flapping hover flight is investigated for (defined by Kurtuluş et al. [1]) elliptic profiles having thicknesses of 12%, 9% and 1% of their chord lengths and compared with those of NACA 0009, NACA 0012 and SD 7003 airfoil profiles all having chord lengths of 0.01m for numerical computations. Computed aerodynamic force coefficients are compared for these profiles having different centers of rotation and angles of attack. The vortex formation, interaction of the leading and trailing edge vortices are represented with vorticiy, pressure coefficient and second invariant of velocity gradient (Q) contours in addition to the streamlines. The shedding of the vortices especially which are coming from the leading edge have different mechanisms for different α_0 parameters, so the aerodynamic force coefficients are mostly influenced by the effect of the angle of attack. NACA profiles have slightly higher lift coefficients than the ellipses of the same t/c ratio. And one of the most important conclusions is that the use of elliptic and NACA profiles with 9% and 12% thicknesses do not differ much as far as the aerodynamic force coefficients is concerned for this Re number regime. But more experimental and computational work is required to understand the thickness effect for even smallest thickness ratios [2].

Another study [46] is performed to analyze the different sinusoidal flapping motion kinematics defined by Wang et al. [3] and Freymuth [4] for different Reynolds numbers in the range of 10^1-10^3 by implementation of the sinusoidal translational and angular motions. Force coefficients and vorticity contours obtained from the experiments [3], [4] and present study are compared.

The sinusoidal motion defined by Wang et al. [3] is applied to a thin wing element of elliptic cross section having a thickness of 12% of its chord. The effects of stroke amplitude and Reynolds number on the aerodynamic force coefficients are investigated. It is observed that the effect of stroke amplitude is more than the effect of Reynolds number on drag coefficient. The computed forces and vorticity distribution obtained from the present study are compared with 3D experimental, 2D numerical and empirical data of Wang et al. [3]. It is observed that the present computational method is good at estimating the force coefficients and the major features of vortex dynamics of the problem. For the same Re number, amplitude (A_0/c) and same 45° angle at the mid-stroke, a comparative study is performed between the flapping motions prescribed by Kurtulus et al. [1] and Wang et al. [3] and it is found that the mean lift coefficient of [1] is twice that of [3].

The sinusoidal flapping motion defined by Freymuth [4] is implemented to an elliptic profile having 1.6mm thickness and 0.0254m chord length. Force coefficients and vortex dynamics obtained from the experiments of Freymuth [4] and present study are compared. Although some parameters are different for numerical and experimental tests good agreement is observed between these two studies.

In this present study the effects of some parameters (e.g. profile shape, thickness, Re, amplitude, etc.) on aerodynamics of flapping motion in hover is put into evidence. The validation of the present computational results with the experimental results available in the literature encourages us to conclude that present numerical method can be a reliable alternative to experimental techniques. The results obtained from the present numerical investigations provided a good description of the unsteady aerodynamic mechanisms for the generation of lift and drag during the flapping motion in hover.

REFERENCE

[1] Kurtulus, D. F., *Numerical and Experimental Analysis of Flapping Motion in Hover. Application to Micro Air Vehicle,* Joint Ph.D thesis Poitiers University/ENSMA (Poitiers France) and METU (Ankara-Turkey), Poitiers, France, 17 June 2005.

[2] Akay B, Kurtulus D.F., Alemdaroglu N., *Unsteady Aerodynamics of Different Wing Profiles at Low Reynolds Number,* NATO AVT-146 Symposium on Platform Innovations and System Integration for Unmanned Air, Land and Sea Vehicles, 14-17 May 2007, Florence, Italy, 2007 .

[3] Wang Z. J., Birch, J. M., Dickinson, M.H., *Unsteady Forces and Flows in Low Reynolds Number Hovering Flight: Two-Dimensional Computations vs. Robotic Wing Experiments,* J. Exp. Biol, 207, pp. 449-460, 2004.

[4] Freymuth, P., *Thrust Generation by an Airfoil in Hover Modes*, Experiments in Fluids, Vol. 9, pp. 17-24, 1990.

[5] Sane, S.P., *The Aerodynamics of Insect Flight, J. Exp. Biol,* 206, pp. 4191-4280, 2003.

[6] Michelson, R., Helmick, D., Reece, S., and Amarena, C., *A Reciprocating Chemical Muscle (RCM) for Micro Air Vehicle "Entomopter" Flight.*

[7] Ansari, S.A., Zbikowski, R., Knowles, K., *Aerodynamic Modeling of Insect-Like Flapping Flight for Micro Air Vehicles*, Progress in Aerospace Sciences 42, 129-172, 2006.

[8] Rare Species Conservatory, "Feathered Facts", http://www.rarespecies.org/kids/feath.htm. (Last accessed date: August 2007)

[9] Ellington, C. P. Philos. Trans. R. Soc. London Ser. B 305, 1, 1984.

[10] Dickinson, M. H., Lehmann, F. O., Sane, S. P., *Wing Rotation and the Basis of Insect Flight, Science*, 284, June 1999.

[11] Wang, J.Z., *Two Dimensional Mechanism of Hovering*, Phys. Rev. Lett. 85, 2216-2219, 2000.

[12] Scientific American, "Catching the Wake", http://www.sciam.com/article.cfm?articleID=00029B82-5453-1C75-9B81809EC588EF21. (Last accessed date: August 2007)

[13] Copy right by Ehrlich, P.R., Dobkin, D.S., Wheye, D., "Hovering Flight", http://www.stanford.edu/group/stanfordbirds/text/essays/Hovering_Flight.html. (Last accessed date: August 2007)

[14] Ellington, C.P., Berg, C., Willmott, P.A., Thomas, A.L.R., *Leading Edge Vortices in Insect Flight*, Nature, 384:626-630, 1996.

[15] Weis-Fogh, T., *Quick Estimates of Flight Fitness in Hovering Animals, Including Novel Mechanisms for Lift Production*, J. Exp. Biol. 59, 169-230, 1973.

[16] Wikipedia-The Free Encyclopedia, "Insect Flight", en.wikipedia.org\wiki\Insect-flight. (Last accessed date: August 2007)

[17] Cranfield University, DCMT - Insect-like Flapping-Wing Micro Air Vehicles.htm

[18] Fitzgerald, R., *Simple Mechanisms Help Explain Insect Hovering*, American Institute of Physics, 2001.

[19] Szmelter J., Zbikowski R., *A Study of Flow Arising from Insect Wing Flapping Motion*, Int. J. Numer. Meth. Fluids, 40:497-505, 2002.

[20] Tuncer, I.H. and Kaya, M., *Optimization of Flapping Airfoils for Maximum Thrust and Propulsive Efficiency*, AIAA Journal, Vol. 43, No. 11, pp. 2329-2336, 2005.

[21] Young, J. and Lai, J.C.S., *Oscillation Frequency and Amplitude Effects on the Wake of a Plunging Airfoil*, AIAA Journal, Vol. 42, No.10, pp. 2042-2052, 2004.

[22] Young, J., *Numerical Simulation of the Unsteady Aerodynamics of Flapping Airfoils*, PhD Thesis, Australian Defence Force Academy, 2005.

[23] Tuncer, İ.H., Walz, R., Platzer, M.F., *A Computational Study on the Dynamic Stall of a Flapping Airfoil*, AIAA-98-2519, 1998.

[24] Willmott AP, Ellington CP., *The Mechanics of Flight in the Hawkmoth Manduca sexta. I. Kinematics of hovering and forward flight*, J. Exp. Biol., 200(21):2705 –2722, 1997.

[25] Willmott AP, Ellington CP., *The Mechanics of Flight in the Hawkmoth Manduca sexta. II. Aerodynamic consequences of kinematic and morphological variation*, J. Exp. Biol.; 200(21): 2723–2745, 1997.

[26] Willmott AP, Ellington CP., *Measuring the Angle of Attack of Beating Insect Wings: Robust three-dimensional reconstruction from two-dimensional images*, J. Exp. Biol., 200(21):2693 –2704, 1997.

[27] Isogai, K., Fujishoro, S., Saitoh, T., Yamamoto, M., Yamasaki, M., Matsubara, M., *Unsteady Three-Dimensional Viscous Flow Simulation of a Dragonfly Hovering*, AIAA Journal, Vol. 42, No. 10, pp. 2053-2059, 2004.

[28] Wu, J.H., Sun, M., *Unsteady Aerodynamic Forces of a Flapping Wing*, J. Exp. Biol. 207. pp. 1137-1150, 2004.

[29] Miller, L.A., Peskin, C.S., *When vortices stick: an aerodynamics transition in tiny insect flight*, J. Exp. Biol, 207, pp. 3073-3088, 2004.

[30] Ramamurti, R., Sandberg, W.C., *A Three-Dimensional Computational Study of the Aerodynamic Mechanism of Insect Flight*, J. Exp. Biol, 205, pp. 1507-1518, 2002.

[31] Lan, S.L., Sun, M., *Aerodynamic Force and Flow Structures of Two Airfoils in Flapping Motions*, Acta Mechanica Sinica (English Series), No.17, pp310-331, 2001.

[32] Sun, M., Tang, J., *Unsteady Aerodynamic Force Generation by a Model Fruit Fly Wing in Flapping Motion*, J. Exp. Biol, 205, pp. 55-70, 2002.

[33] Wang, J.Z., *Vortex Shedding and Frequency Selection in Flapping Flight*, Journal of Fluid Mech., 410,323-341, 2000.

[34] Eldredge, J.D., *Efficient Tools for the Simulation of Flapping Wing Flows*, 43rd Aerospace Sciences Meeting, January 10–13, Reno, NV. AIAA 2005-0085, 2005.

[35] Poelma, C., Dickson, W.B., Dickinson, M.H., *Time-resolved reconstruction of the full velocity field around a dynamically-scaled flapping wing*, Experiment in Fluids, 41: 213-225, 2006.

[36] Tian, X., Iriarte, J., Middleton, K., Galvao, R., Israeli, E., Roemer, A., Sullivan, A., Song, A., Swartz, S., Breuer, K., *Direct Measurement of the Kinematics and Dynamics of Bat Flight*, 36th AIAA Fluid Dynamics Conference and Exhibit, 5-8 June, San Francisco, California, 2006.

[37] Lehmann, F.O., Sane, S.P., Dickinson, M. H., *The Aerodynamic Effect of Wing-Wing Interaction in Flapping Insect Wings*, J. Exp. Biol. 208. pp. 3075-3092, 2005.

[38] Galvao, R., Israeli, E., Song, A., Tian, X., Bishop, K., Swartz, S., Breuer, K., *The Aerodynamics of Compliant Membrane Wings Modeled on Mammalian Flight Mechanics*, 36th AIAA Fluid Dynamics Conference and Exhibit, 5-8 June, San Francisco, California, 2006.

[39] Singh, B., Ramasamy, M., Chopra, I., Leishman, G.J., *Experimental Studies on Insect-Based Flapping Wings for Micro Hovering Air Vehicles*, AIAA, 2005.

[40] Usherwood, J.R., Hedrick, L.T., McGowan, C.P., Biewener, A.A., *Dynamic Pressure Maps for Wings and Tails of Pigeons in Slow, Flapping Flight, and Their Energetic Implications*, J. Exp. Biol. 208. pp. 355-369, 2005.

[41] Dickinson, M. H., Götz, K.G., *Unsteady Aerodynamic Performance of Model Wings at Low Reynolds Number*, J. Exp. Biol. 174, 45-64, 1993.

[42] Spedding, G.R., Rosen, M., Hedenström, A., *A Family of Vortex Wakes Generated by a Thrush Nightingale in Free Flight in a Wind Tunnel Over Its Entire Natural Range of Flight Speeds,* J. Exp. Biol, 206, pp. 2313-2344, 2003.

[43] Platzer, M. F., Jones, K. D., *Flapping Wing Aerodynamics-Progress and Challenges*, AIAA-06-0500, Reno, Nevada, 2006.

[44] Pivkin, I.V., Hueso, E., Weinstein, R., Laidlaw, D.H., Swartz, S., Karniadakis, G.E., *Simulation and Visualization of Air Flow around Bat Wings during Flight*, V.S. Sunderam et al. (Eds.): ICCS 2005, LNCS 3515, pp. 689 – 694, 2005.

[45] STAR-CD User Guide, Computational Dynamics Limited, 2002.

[46] Akay B, Kurtulus DF, Alemdaroglu N., *Parametrical Study of Sinusoidal Flapping Motion Aerodynamics*, 4th Ankara International Aerospace Conference, Ankara, Turkey, (accepted), 2007.

[47] Freymuth, p., Bank, W., Palmer, M., *Use of Titanum tetra-chloride for flow visualization of accelerating flow around airfoils.* In Flow Visualization III. (ed. Yang, W.-J.). Pp.99-105. Washington: Hemisphere, 1985.

[48] Kurtulus, D.F., Akay, B., Alemdaroglu H.N., *Çırpma Hareketi Aerodinamiğinin İki Boyutlu Silindir Kullanılarak İncelenmesi*, (in Turkish), Proceeding of HaSeM'06 Kayseri 6th Aeronautical Symposium, HaSeM-E130, Nevşehir, Turkey, 12-14 May 2006.